UCSF
UC San Francisco Electronic Theses and Dissertations

Title
Exploring the function of fast spiking interneurons in the striatum

Permalink
https://escholarship.org/uc/item/0wk1c05d

Author
Liu, Max Hao

Publication Date
2019

Peer reviewed|Thesis/dissertation

eScholarship.org Powered by the California Digital Library
University of California

Exploring the function of fast spiking interneurons in the striatum

by
Max Hao Liu

DISSERTATION
Submitted in partial satisfaction of the requirements for degree of
DOCTOR OF PHILOSOPHY

in

Neuroscience

in the

GRADUATE DIVISION
of the
UNIVERSITY OF CALIFORNIA, SAN FRANCISCO

Approved:

DocuSigned by:
Michael P. Stryker
6F464CB16FDD412...

Michael P. Stryker
Chair

DocuSigned by:
Christoph Schreiner, MD, PhD

DocuSigned by:
Vikaas Sohal

Vikaas Sohal

DocuSigned by:
Anatol Kreitzer
03F45B9A4CF445E...

Committee Members

COPYRIGHT 2019
by
Max Hao Liu

ACKNOWLEDGEMENTS

The work presented in this thesis was a product of hundreds of hours of recordings, dozens of mice, and many weekends and nights spent poring over Matlab code. As much work as I have put into these projects, they are also a product of the support, instruction, and mentorship I have received here at my time in UCSF, and over the course of my life. Without the people and institutions providing this support, none of this work would have been possible.

I would first like to thank the members of my thesis committee, Michael Stryker (the chair of the committee), Vikaas Sohal, and Christoph Schreiner. From the preparation for my qualifying exam to my last committee meeting, they have provided sound and thoughtful scientific insights and suggestions, and often pushed me to better understand my work. Beyond their scientific contributions, I greatly appreciate their enthusiasm during our committee meetings and one-on-one discussions. At many points where I felt like a year had been wasted, my committee was always eager to point out the relevance of what I had done, and to seek a path forward that was practical and realistic.

Next, I would like to thank my advisor, Anatol Kreitzer, for his mentorship over the past five years. During my PhD, Anatol gave me unlimited intellectual freedom, allowing me to pursue my interests, even if they ended up leading to a strange corner of the striatum. I cannot emphasize enough how this has been a crucial part of my growth during my PhD. Anatol has also never wavered in stating his belief in my ability to contribute scientifically to the lab, even when I have doubted my choice of pursuing a PhD. This confidence has been encouraging in some of the lower points of my

research. Finally, Anatol has a special talent for selecting and attracting excellent scientists, who have contributed greatly to my development over the course of my PhD. Of my lab members, I have to give especial thanks to several individuals.

First, I want to thank Andrew Moses Lee, who went out of his way to make sure I would have space, mice, and a useful project.

Second, I want to thank Thomas Roseberry, who was one of the first people I worked with in the lab. Tom's irrepressible enthusiasm, and his willingness to teach me, and generosity with his time and his rig shaped the beginning of my time in the lab.

Third, I want to thank Alexandra Nelson, who has become an important mentor and advisor. Her generosity with her time and energy, whether to resolve a scientific problem or discuss challenges I was facing with graduate school, are a gift I can never repay.

Fourth, I want to thank Scott Owen, with whom I collaborated on the work presented here in the first chapter of my thesis. Working with Scott has certainly been an invaluable lesson in how to organize, execute, and publish a set of experiments. His enthusiasm and energy make him an exemplar to be emulated.

Fifth, I want to thank Anthony Lien, who has become a close friend, a trusted scientific advisor, and a wonderful lunch buddy. Tony has a vast fund of knowledge from which he is always willing to contribute. His willingness to dive deeply into a literature in order to gain a better understanding of the science is inspiring. So too is his generosity with his time, energy, and expert technical skills. The work presented in the second chapter of my thesis largely sprang from his willingness to sort through my raw data with me, and his sharp eye for interesting results.

I also owe my other labmates thanks, including Ben Margolin, without whom I would be mouse-less and without data, and who has humored my attempts at mentorship; Selin Schamiloglu, who has been a great friend and a patient running buddy; and Arnaud Lalive, for his cheerfulness, his advice, and his generosity with setting up a range of behaviors.

Outside of the lab, I want to thank my MSTP classmates, who I have come to SF with from the start. I especially want to thank Allison Wong and Tess Veuthey, for keeping me relatively healthy and relatively sane, respectively.

I have been lucky to be in a relationship with the wonderful Grace Ha for as long as my PhD, and I owe her many thanks for her patience, kindness, and understanding. I have learned so much from her, and hope to continue learning more in the future.

Finally, I must thank my family, without whom I wouldn't exist. I want to thank my sister, Anne Liu, for always being there, and for being a role model to aspire to. I want to thank my parents, Hong Wu and Xin Liu, for their patience, support, and sage advice that I wish I had taken more often.

The work in Chapter 2 was performed in collaboration with co-author Scott F. Owen, and is in part, a reprint of the material as it appears in: Owen, S.F., Liu, M.H, and Kreitzer, A.C. (2019) Thermal constraints on in vivo optogenetic manipulations. *Nature Neuroscience*, doi: 10.1038/s41593-019-0422-3 . In this work, SFO and MHL designed experiments, performed analyses, made figures and wrote the manuscript. MHL performed *in-vivo* recordings of physiology and temperature, as well as behavioral experiments. SFO performed slice recordings and temperature modeling work.

ABSTRACT

Exploring the function of fast spiking interneurons in the striatum

by Max Hao Liu

Fast spiking interneurons (FSIs) are thought to play a critical role in the normal function of the striatum, which is the input nucleus to the basal ganglia. *In vitro* studies have determined that FSIs are a major source of inhibition onto striatal principal cells, or medium spiny neurons (MSNs). However, *in vivo* studies have produced conflicting results regarding how FSI activity modulates MSN activity in the awake animal. Here, we use optogenetic techniques and acute head-fixed extracellular recordings to resolve existing controversy in our understanding of FSI-MSN interactions. We find that the net effect of FSI activity is to suppress MSNs, and in the process, discover an opsin-independent effect of light on physiology and behavior. We find strong evidence that this effect is mediated by temperature, and determine parameters for the safe use of light in neuroscience experiments. We then investigate the specific manner in which FSIs influence MSN activity by recording the sensory responses of striatal units in the auditory striatum. Here, we find that MSNs are more frequency selective for pure tone stimuli than neighboring FSIs, and exhibit differences in their responses to continuous stimuli when compared with FSIs. Optogenetic inhibition of FSIs results in a disinhibition of MSN responses to pure tones, increasing the magnitude of their responses and reducing their frequency selectivity. These results suggest that FSI activity in the auditory striatum serves to shape the activity of surrounding MSNs and increase their frequency selectivity.

Table of Contents

CHAPTER 1

INTRODUCTION..... 1

The input nucleus of the basal ganglia: the striatum..... 1

In vitro feed forward inhibition by striatal fast spiking interneurons onto medium spiny neurons..... 2

The in vivo function of striatal fast spiking interneurons remains unclear..... 3

CHAPTER 2

EVALUATING THE IN VIVO ROLE OF STRIATAL FSIS AND UNCOVERING THERMAL CONSTRAINTS ON OPTOGENETIC MANIPULATIONS..... 5

INTRODUCTION:..... 5

RESULTS:..... 6

Optogenetic inhibition of striatal PV+ interneurons disinhibits MSNs in two PV-Cre mouse lines..... 6

Light is sufficient to suppress striatal firing rates in vivo without opsin expression..... 7

Opsin-independent suppression of MSNs by 15 mW of light overcomes the disinhibition arising from optogenetic silencing of PV+ interneurons..... 8

Light suppresses activity of neurons in striatum and other brain regions..... 8

Light modulates firing rates in striatum via changes in temperature..... 9

Light mediated current is an inwardly rectifying potassium current..... 11

Light drives behavioral change..... 12

DISCUSSION:..... 13

Striatal FSIs suppress MSNs in vivo..... 13

Light alone is sufficient to suppress the neuronal activity in striatum and other brain regions..... 13

Suppression of Striatal Units by Light is Mediated Temperature Modulation of an Outward Potassium Current *14*

Light drives temperature shifts that alter neuronal activity and behavior *15*

CONCLUDING REMARKS 17

MATERIALS AND METHODS: 19

CHAPTER 3

INVESTIGATING THE ROLE OF FSIS IN SHAPING MSN RESPONSES IN AUDITORY STRIATUM 40

INTRODUCTION: 40

RESULTS: 43

MSNs and FSIs respond to pure tone auditory stimuli *43*

MSNs and FSIs respond to continuous auditory stimuli *45*

Optogenetic Inhibition of FSIs in Auditory Striatum Disinhibits MSN Auditory responses .. *47*

DISCUSSION: 49

FSIs respond to pure tones like surrounding MSNs, while exhibiting broader frequency tuning and lower thresholds for activation *49*

FSIs and MSNs respond to DMR stimuli, but have divergent breadth of frequency tuning. *50*

Optogenetic suppression of FSIs disinhibits MSN tone responses *51*

CONCLUDING REMARKS 53

MATERIALS AND METHODS: 56

REFERENCES: 72

LIST OF FIGURES

FIGURE 2. 1 OPTOGENETIC INHIBITION OF STRIATAL PV+ INTERNEURONS PRODUCES DISINHIBITION OF MSNS IN TWO PV-CRE LINES. 30

FIGURE 2. 2 LASER LIGHT ALONE IS SUFFICIENT TO INDUCE SUPPRESSION OF NEURONAL FIRING RATES IN-VIVO WITHOUT OPSIN EXPRESSION. 32

FIGURE 2. 3 OPSIN-INDEPENDENT SUPPRESSION OF MSNS BY 15 MW OF LIGHT OVERCOMES DISINHIBITION ARISING FROM OPTOGENETIC SILENCING OF PV+ INTERNEURONS. 33

FIGURE 2. 4 LIGHT DELIVERY SUPPRESSES MSN ACTIVITY *IN VIVO* AND IN ACUTE SLICES..... 34

FIGURE 2. 5 LIGHT-INDUCED HEATING INCREASES AN INWARDLY-RECTIFYING POTASSIUM CONDUCTANCE IN MSNS. 35

FIGURE 2. 6 LIGHT ILLUMINATION OF DORSAL STRIATUM DRIVES BEHAVIORAL CHANGE. 37

FIGURE 2.S 1 TIME-COURSE OF LIGHT-DRIVEN TEMPERATURE CHANGES. 39

FIGURE 3. 1 FSIS AND MSNS RESPOND TO PURE TONE STIMULI..... 64

FIGURE 3. 2 FSIS AND MSNS EXHIBIT RESPONSES TO DYNAMIC MOVING RIPPLE STIMULI..... 65

FIGURE 3. 3 RIPPLE TRANSFER FUNCTIONS OF FSIS AND MSNS REVEAL DIFFERENCES IN PREFERENCES FOR SPECTRAL AND TEMPORAL MODULATION. 66

FIGURE 3. 4 OPTOGENETIC INHIBITION OF FSIS PRODUCES DISINHIBITION OF MSNS..... 67

FIGURE 3.S 1 TUNING WIDTHS ACROSS AMPLITUDES FOR FSIS AND MSNS WITH THRESHOLD AMPLITUDE EQUAL TO OR LESS THAN 30 DB SPL..... 69

FIGURE 3.S 2 DIFFERENCES IN LATENCY FOR FSIS AND MSNS. 70

FIGURE 3.S 3 EXAMPLES OF EFFECTS OF OPTOGENETIC INHIBITION OF FSIS. 71

CHAPTER 1

INTRODUCTION

The input nucleus of the basal ganglia: the striatum

The basal ganglia are a series of interconnected subcortical nuclei important for movement, decision-making, and learning. Through the input nucleus, the striatum, the basal ganglia receive inputs from across the brain, including many cortical and thalamic regions that provide external information such as sensory signals, as well as internal information about behavioral state, motor status and reward expectation (Bolam et al., 2000, Kincaid et al., 1998, Smith et al., 1994, Wall et al., 2013). Integrated within the striatum and other basal ganglia nuclei, these inputs ultimately influence output nuclei that project to motor regions including the superior colliculus (Hikosaka and Wurtz, 1983), mesencephalic locomotor region (Roseberry and Lee et al., 2016), and motor thalamus (Kim et al. 2017, Lalive et al. 2018). Through these outputs, the basal ganglia can influence a range of behaviors, including orienting, eye movements, locomotion, complex movements, and decision-making.

As the gateway to the basal ganglia, the striatum plays a critical role in the control and processing of information entering the basal ganglia. Approximately 90% of neurons within the striatum are medium spiny neurons, or MSNs. These principal cells are the only striatal cells to project to downstream nuclei (Kemp and Powell, 1971, Rymar et al., 2004). Therefore, any information that passes through the striatum to the rest of the basal ganglia must pass through these MSNs. MSNs are divided between direct and indirect pathway MSNs, which project either directly or indirectly to basal ganglia output nuclei (Smith et al., 1998). These different types of MSNs are hypothesized to influence behavior in different ways, with the direct pathway promoting movement, and the indirect pathway suppressing movement (Albin et al., 1989). This “classical model” of the basal ganglia has been supported by optogenetic experiments (Kravitz

et al., 2010), though recording studies of direct and indirect pathway neurons has suggested that the function of these two pathways may be more complex (Cui et al., 2013).

MSNs receive inhibitory input from a range of sources. First, MSNs have axon collaterals that project to neighboring MSNs, and therefore receive inhibition from neighboring MSNs, though these connections are individually very weak (Tepper et al., 2004). Second, MSNs receive long range inhibitory inputs from cortical regions, including prefrontal (Lee et al., 2014), motor, and somatosensory brain regions (Rock et al., 2016). These projections have been reported to influence activity and behavior (Lee et al., 2014), though their overall contribution to striatal inhibition is unclear. Finally, MSNs receive inhibitory inputs from a range of GABAergic interneurons within the striatum, the most prominent of which are fast spiking (FSI) and persistent and low-threshold spike (PLTS) interneurons (Tepper et al., 2004). As FSIs are thought to provide the majority of inhibitory input onto MSNs, we will focus on their role in regulating MSN activity.

In vitro feed forward inhibition by striatal fast spiking interneurons onto medium spiny neurons

FSIs make up several percent of total striatal neurons, and are distributed throughout the striatum, with increased density of FSIs in lateral regions of striatum. FSIs receive excitatory inputs from cortex and thalamus (Kita 1993, Lapper et al., 1992). In contrast to MSNs, which receive few synapses from many inputs, FSIs appear to have more synaptic connections with each input (Ramanathan et al., 2002). FSIs connect to each other, both by gap junctions (Kita et al., 1990, Koos and Tepper, 1999) and by GABAergic synapses (Gittis et al., 2010).

Acute slice recordings have determined that FSIs maintain strong inhibitory connections to neighboring MSNs with high connection probability (Koos and Tepper, 1999, Mallet et al., 2005, Gittis et al., 2010), and have axonal projections that densely innervate MSNs within a 300 um radius (Gittis et al., 2010, Straub et al., 2016). FSIs are estimated to project to 135-541

neighboring MSNs, and each MSN is thought to receive inhibitory inputs from 4-27 FSIs (Koos and Tepper, 1999). FSIs are thought to provide feedforward inhibition onto MSNs, as they are activated earlier (Parthasarathy and Graybiel, 1997) and with lower intensity of cortical electrical stimulation (Mallet et al., 2005). More recently, recordings in a slice preparation preserving cortical input structure has confirmed this hypothesis (Owen et al., 2018). This work found that activation of cortical afferents produces excitation paired with inhibition onto downstream MSNs, with inhibition slightly lagging excitation. This inhibitory current was then abolished by optogenetic silencing of FSIs, indicating that FSIs are responsible for this disynaptic feed-forward inhibition.

Function of striatal fast spiking interneurons *in vivo* remains unclear

Despite their clear importance in providing inhibition onto MSNs, *in vivo* studies of FSIs have generated conflicting results regarding their function. Cross-correlograms, a standard method for detecting monosynaptic inhibition in other brain regions, detect FSI-MSN interactions in only a minute fraction of potential pairs, far below expected connection rates (Gage et al., 2010, Bakhurin et al., 2016). This work and others have led to suggestions that FSI activity may require synchrony to affect MSN firing (Gage et al., 2010), that effects of FSI activity may be heterogeneous (O'Hare et al., 2017), or that it may only occur under specific network states (Burguière et al., 2013).

Adding to this confusion, two recent publications utilizing optogenetic tools to suppress FSIs have arrived at fundamentally different conclusions. One study finds that FSI suppression leads to MSN disinhibition, consistent with FSI activity suppressing that of MSNs (Owen et al., 2018). In contrast, another study finds that suppressing FSI activity paradoxically inhibits neighboring MSNs. Based on these results, the authors propose a disinhibitory circuit by which FSIs suppress the activity of other striatal interneurons to activate MSNs (Lee et al., 2017).

This thesis seeks to shed light upon the following question: How does the *in vivo* activity of FSIs modulate the activity of MSNs? In the first chapter, we will resolve the existing controversy regarding the net effect of FSI activity on that of surrounding MSNs. We not only find that FSIs suppress the activity of MSNs, but also that light alone can generate physiological and behavioral changes via the temperature sensitivity of an inwardly rectifying potassium conductance. This finding has broad implications for the use of light in neuroscience experiments in general. In the second chapter, we examine the specific manner in which FSI activity modulates that of MSNs by using sensory inputs to investigate the selectivity of striatal neurons. Using the auditory striatum as a sensory preparation, we find that FSIs and MSNs have different response properties to both pure tone and continuous stimuli, and that MSNs are more selective in their auditory responses. Optogenetic silencing of FSIs results in a disinhibition of surrounding MSNs, which produces a decrease in the selectivity of their frequency responses. These results suggest that FSI activity serves to increase the selectivity of MSN responses.

CHAPTER 2:

Evaluating the in vivo role of striatal FSIs and uncovering thermal constraints on optogenetic manipulations

INTRODUCTION:

Previous studies in brain slices have established that FSIs form strong GABAergic connections onto neighboring MSNs with a high connection probability (Gittis et al., 2010, Koós and Tepper, 1999, Planert et al., 2010). While these connections are sufficient to alter MSN spike timing in the slice (Koós and Tepper, 1999), inhibition by FSIs has proven remarkably difficult to detect in vivo, leading to the suggestion that individual FSI spikes may not be sufficient to suppress MSN spiking (Gage et al., 2010), that FSI suppression of MSNs may be heterogeneous (O'Hare et al., 2017), or that it may be effective only in particular network states (Burguière et al., 2013).

Most strikingly, two recent studies using ostensibly similar optogenetic approaches arrived at opposite conclusions regarding the physiological consequences of silencing these interneurons in the adult mouse brain (Owen et al., 2018, Lee et al., 2017). Here we test how choice of mouse line and light power can affect the apparent response of MSNs to optogenetic silencing of FSIs. Our results demonstrate that when optogenetic silencing is specifically targeted for FSIs, the net result is to disinhibit neighboring MSNs. However, we also show that light can interact directly with both MSNs and FSIs to suppress their activity independent of opsin expression. At high light power (~15 mW) the non-specific mechanism predominates, occluding and reversing the disinhibition of MSNs that follows optogenetic suppression of FSIs. A shift in the balance between these two physiological mechanisms is the most parsimonious explanation for the discrepancy between these two reports. Finally, we demonstrate that this

light-mediated suppression of activity is present in a range of brain regions, is dependent upon an outward potassium current in striatum, and is sufficient to alter mouse behavior. These findings provide a set of guidelines for the appropriate use of light in optogenetic and imaging experiments.

RESULTS:

Optogenetic inhibition of striatal PV+ interneurons disinhibits MSNs in two PV-Cre mouse lines

Two of the Parvalbumin-cre mouse lines most commonly used to label FSIs (PV-2A-cre and PV-Arbr-cre) capture different proportions of these interneurons in the striatum, with the Arbr line capturing ~40%, while the 2A line captures ~80% of PV+ striatal neurons (Hippenmeyer et al., 2005, Madisen et al., 2010). Given this vast difference in penetrance, we hypothesized that differences between the two transgenic lines could account for the striking discrepancy in physiological responses between two studies that recently used these lines to optogenetically silence striatal FSIs (Lee et al., 2017, Owen et al., 2018). For example, silencing a varying proportions of FSIs might have different network effects, or the Arbr line might be selecting for a specific subset of FSIs within the striatum.

To test this, we performed a direct comparison between these mouse lines. Adeno-associated virus encoding halorhodopsin under a cre-dependent promoter (AAV-DIO-eNpHR3.0) was injected into dorsal striatum of adult mice. Acute head-fixed recordings were performed 6-8 weeks after virus injection to allow for adequate halorhodopsin expression (Figure 2.1A-D; (Mattis et al., 2012)). Isolated single units were identified as putative MSNs and FSIs based on established waveform and firing rate criteria (Figure 2.1E, see methods) (Gage et al., 2010, Lee et al., 2017).

Activation of eNpHR3.0 by green light delivered through a 200 mm fiber attached to the recording electrode (3 mW at 532nm for 2 seconds) suppressed a large proportion of physiologically-identified FSIs. The modulation of FSIs was not statistically different between Cre lines (Figure 2.1F-G). Silencing of FSIs disinhibited neighboring MSNs in both mouse lines (Figure 2.1H-I), with stronger modulation in the PV-2A-cre line. This is consistent with recently published results in freely moving animals in striatum (Owen et al., 2018), and with FSI silencing in other brain regions (Royer et al., 2012, Sachidhanandam et al., 2016, Atallah et al., 2012), but contrasts with at least one report using head-fixed recordings from the dorsal striatum in the PV-Arbr-cre mouse line (Lee et al., 2017). Surprisingly, we also found weak but statistically significant suppression of both FSI and MSN activity during light delivery in control animals that received a fluorophore-only virus with no opsin (Figure 2.1F, H).

Light is sufficient to suppress striatal firing rates in vivo without opsin expression

To test how light delivery affects the activity of striatal MSNs *in vivo*, we performed acute single-unit recordings from in the dorsal striatum of awake, head-fixed, wild-type mice in the absence of any opsin or fluorophore expression (Figure 2.2A). Within a recording session, 532 nm light was delivered in blocks of 50 trials at either 3 or 15 mW for a total of 200 trials. Consistent with our previous set of control recordings, light delivery through a 200 mm optical fiber affixed to the dual-shank recording probe 750 mm above the recording sites reversibly suppressed spiking activity in FSIs and MSNs within 1-2 seconds (Figure 2.2B,C). This finding is consistent with the hypothesis that light is capable of modulating neuronal activity in a power-dependent manner.

Opsin-independent suppression of MSNs by 15 mW of light overcomes the disinhibition arising from optogenetic silencing of PV+ interneurons

The opsin-independent suppression of MSN firing (Figure 2.2C) highlights a major potential confound in the interpretation of these experiments. We therefore tested whether this direct light-induced suppression of MSN firing could interfere with the ability to detect the disinhibition of MSNs that follows optogenetic silencing of striatal FSIs. To control for variability across animals and recording sessions, each recording session included blocks of 3 mW and 15 mW light in PV-Arbr-cre mice. Masking lights were omitted in the 15 mW condition to more precisely replicate the experimental configuration in Lee et al (Figure 2.3A; (Lee et al., 2017)).

FSIs were silenced in both 3 mW and 15 mW conditions, and were significantly more inhibited by 15 mW laser light (Figure 2.3B). Suppression of FSIs with 3 mW resulted in disinhibition of neighboring MSNs (Figure 2.3C, top left) in a data set that is consistent with but independent from the one reported above (Figure 2.1H). Increasing the light power to 15 mW within the same recording reversed the disinhibition and caused a net suppression of MSN firing (Figure 2.3C). In the absence of masking lights, we also observed a transient excitation of MSNs at the onset of the laser pulse, resulting in a physiological response that closely parallels previously reported results (Lee et al., 2017): brief excitation followed by a slowly emerging inhibition (Figure 2.3C, bottom left).

Light suppresses activity of neurons in striatum and other brain regions

We considered several explanations for this light-induced suppression of activity in wild-type MSNs, including physiological responses to local heating of brain tissue, sensory responses to light detection at the back of the retina, or artifacts caused by interactions between the light delivery and recording systems. To rule out the latter two possibilities, we tested whether equivalent physiological responses could be detected in an acute slice preparation,

where most afferent connectivity has been severed and the recording system is entirely different.

We obtained whole-cell recordings from MSNs in acute slices prepared from wild-type mice using a potassium-based internal solution (Figure 2.4A). A current injection through the recording pipette elicited spiking in MSNs, which are otherwise quiescent in a slice preparation (Figure 2.4B, left). To maintain consistency with the *in vivo* recording preparation, light was delivered through an optical fiber 200 mm in diameter placed 500-800 mm from the recorded neuron. In agreement with the *in vivo* results, light delivery at low power (3 mW) caused a modest but statistically significant drop in firing rate, while higher power (15 mW) reduced spiking more markedly (Figure 2.4C,D).

To investigate whether this light-induced suppression of neuronal activity is specific to striatal MSNs, we repeated this whole-cell recording experiment in other cell types in the hippocampus and cortex. Spiking activity in CA1 pyramidal neurons was unaffected by light delivery at 15 mW, while dentate gyrus granule cells and cortical layer 5 pyramidal neurons were modestly suppressed (Figure 2.4E-G). Cortical layer 5 fast-spiking interneurons were strongly suppressed by light. These findings are consistent with a recent publication that reached similar conclusions in an overlapping set of brain regions (Ait Ouares et al., 2019).

Light modulates firing rates in striatum via changes in temperature

We hypothesized these physiological responses to light delivery in wild-type MSNs could arise from local heating of brain tissue. To measure the extent of this heating in vivo, we acutely inserted a miniaturized thermocouple probe in the place of the recording electrode. As predicted by published computer models and measurements in other brain regions (Stujenske et al., 2015, Arias-Gil et al., 2016), light delivery through the optical fiber caused a transient, monotonic increase in temperature at the recording site of up to 2°C (Figure 2.5A,B, 1.S1A).

The time-course of this temperature change, when fit with a single exponential (Figure 2.5B), matched closely with the time-course of the decrease in MSN firing (Figure 2.5C).

To investigate the physiological mechanism underlying this light-induced suppression of spiking activity in wild-type MSNs, we recorded a set of MSNs in voltage-clamp at a holding potential of -50 mV using a potassium-based internal solution (Figure 2.5D). Light delivery at 3 mW caused a modest (~0.2 °C) increase in temperature and elicited a slowly-activating outward current (Figure 2.5D-G). Increasing the light power to 15 mW caused a larger (~1 °C) temperature change and significantly increased the size of this current.

To test whether this temperature change was sufficient to elicit the observed outward current independent of light delivery, we set up a custom-built system to change the temperature in acute slices locally and rapidly without disturbing the stability of our whole-cell recordings (Figure 2.5H). Using the same thermocouple for calibration, we found this system capable of heating the slice by 1.92 °C (hot) or 0.89 °C (warm), depending on the heat setting (Figure 2.5I). When ice-water was used for cooling, the temperature of the slice was reduced by -2.82 °C (cold).

We used whole-cell recordings to measure the physiological consequences of this temperature change in MSNs voltage-clamped at -50 mV with a potassium-based internal recording solution. Transiently warming the slice elicited an outward current that was graded by temperature and followed a time-course that closely tracked the measured temperature change (Figure 2.5J). In contrast, cooling of the slice caused an apparent reduction in this outward current. Plotting the temperature-evoked current against the amplitude of the temperature change in each group revealed a strikingly linear relationship between temperature and current, suggesting temperature-dependent modulation of a tonically active current (Figure 2.5K).

To better understand the relationship between light delivery and local heating of brain tissue underlying these physiological effects, we turned to a recently published computer model (Stujenske et al., 2015) to predict the local temperature change in response to light delivery as a function of power and light pulse duration (Figure 2.5L). This plot includes a "threshold" line at a temperature change of approximately 0.1 °C, which corresponds to the intensity and duration at which we begin to observe minimal effects of light-driven heating on the physiology of wild-type MSNs (Figure 2.1; 3 mW for 1 sec). These modeling results highlight an important distinction between expected temperature changes in response to very short (10 ms) as opposed to very long light (30 sec) pulses. High light power in excess of 30 mW is expected to cause minimal heating if pulse durations are shorter than 100 ms. However, if continuous light is delivered for longer periods, as is commonly used for optogenetic inhibition experiments, significant heating of brain tissue will occur even at modest laser powers (3-5 mW), increasing the potential for off-target physiological effects. This model was similarly informative in describing how changes in duty cycle, pulse frequency, and wavelength affect expected temperature changes the interactions between duty cycle, duration, frequency, power, and wavelength for single light pulses, and pulse trains (Figures 1.S1D,E).

Light mediated current is an inwardly rectifying potassium current

To characterize the physiology of this light-evoked current, we performed additional whole-cell recordings in which we varied the holding potential of the voltage-clamped MSN between -140 mV and -50 mV (Figure 2.5M-O). Consistent with light-induced activation of a potassium conductance, the current reversed at -93 mV. The curve also showed a striking inward rectification (Figure 2.5O). This light-induced current was almost entirely abolished in MSNs recorded using a cesium-based internal solution (Figure 2.5P, top). Furthermore, in MSNs recorded with a potassium-based internal, the light-induced current was sensitive to bath application of $BaCl_2$ at a concentration of 250 mM (Figure 2.5Q,R). These physiological and

pharmacological results are most consistent with light-evoked activation of an inwardly rectifying potassium channel (Figure 2.5D-Q).

Light drives behavioral change

Finally, we tested whether this light-driven suppression of MSNs can affect animal behavior (Figure 2.6A-C). We implanted optical fibers into the dorsal striatum of wild-type mice and delivered light unilaterally to one hemisphere per session while measuring rotations and locomotor behavior using standard open-field protocols (see methods) and automated tracking of body position with DeepLabCut (Mathis et al.,2018). Consistent with transient suppression of striatal network activity, light delivery elicited a reversible, light power-dependent shift in rotational behavior in the direction ipsilateral to the illumination, measured as either change in rotational bias or direction change of the mouse (Figure 2.6D-F). These alterations of rotational behavior did not affect average instantaneous speed, total rotations, distance traveled, or binned speed values (Figure 2.6G-J)

DISCUSSION:

Striatal FSIs suppress MSNs *in vivo*

We performed a series of in vivo and in vitro experiments designed to address a surprising discrepancy between recent optogenetic studies of striatal FSI function (Lee et al., 2017, Owen et al., 2018). Our results unambiguously indicate that silencing FSIs disinhibits neighboring MSNs, consistent with a role of FSIs in delivering feed forward inhibition to the striatum (Owen et al., 2018, Mallet et al., 2005, Koós and Tepper, 1999). Using ~3 mW of 532 nm light, we demonstrate optogenetic suppression of striatal FSIs and disinhibition of MSNs in two different mouse lines. Furthermore, we demonstrate that within the same recording, when we switch from 3 mW to 15 mW laser power (mimicking the experimental protocol of Lee et al., 2017), the effect of the laser stimulation shifts from MSN disinhibition to MSN suppression. In 15 mW laser trials, the response of MSNs to the laser closely matches those in a recent publication finding that FSI suppression leads to MSN inhibition (Lee et al., 2017), suggesting that high laser powers may be responsible for their experimental findings.

Light alone is sufficient to suppress the neuronal activity in striatum and other brain regions

Having found that light alone is sufficient to suppress activity of striatal units in vivo, we performed ex vivo experiments in striatum, hippocampus, and cortex, to determine whether this light-dependent suppression is found in other brain regions. We found that light suppresses neuronal activity in striatum, cortex, and dentate gyrus. The suppression of cortical pyramidal neurons in acute slices was surprising with respect to previous reports that light-driven temperature changes cause a net increase in cortical activity *in vivo* (Stujenske et al., 2015). However, given that the suppression of these interneurons was stronger than that of neighboring pyramidal neurons (Figure 2.1M), the light-driven elevation of cortical neurons reported *in vivo* (Stujenske et al., 2015) may arise from disinhibition through light-driven

suppression of neighboring inhibitory interneurons. This highlights an interesting potential mechanism by which temperature modulation of cortex influences neuronal activity. Further investigation of this effect is warranted to better understand the nature of temperature based modulation of cortical regions (Long and Fee, 2008).

Suppression of Striatal Units by Light is Mediated Temperature Modulation of an Outward Potassium Current

One documented mechanism for light to influence neuronal activity is change in temperature (Stujenske et al., 2015). To determine if this was the case in striatum, we performed a series of slice experiments to characterize the suppression of striatal activity. Using voltage clamp recordings, we determined that both light and temperature change induce an outward current. This current has a reversal potential around -90 mV, is inwardly rectifying, and is sensitive to both intracellular cesium and extracellular barium.

Neurons throughout the brain express distinct complements of potassium channels. The conductance of several potassium channel subtypes is temperature-dependent, including the K_V voltage-gated (Yang and Zheng, 2014), K_{2P} two-pore (Schneider et al., 2014), and K_{Ca} calcium-activated (Wawrzkiewicz-Jałowiecka et al., 2017) subtypes. However, both K_V and K_{2P} channels are outwardly rectifying, and K_{2P} channels are insensitive to block by barium or cesium (Lesage, 2003, Patel and Honoré, 2001). Among calcium-activated K_{Ca} channels, small-conductance (SK) channels are inwardly rectifying (Soh and Park, 2001) but large-conductance (BK) K_{Ca} channels are not (Brelidze et al., 2003). However, while BK channel conductance is increased at elevated temperatures (Yang and Zheng, 2014), evidence for temperature-dependence of SK channels is sparser. The light-activated current that we recorded was insensitive to bath application of the SK channel blocker Apamin (data not shown), suggesting this current most likely does not derive from temperature-dependent modulation of SK channels. Inwardly

rectifying K_{ir} channels are expressed in MSNs where they regulate spiking (Rothwell et al. 2014). Thermo-sensitivity has been suggested for K_{ir} inwardly rectifying channels, based on structural homology to thermoTRP channels (Yang et al. 2014). Although the pharmacology for these channels is sparse and not especially effective, sensitivity to barium or cesium is a primary hallmark of K_{ir} channels (Figure 2.5P). Furthermore, light-mediated suppression of spiking appears to be restricted to brain regions that express K_{ir} channels, including dentate gyrus, cortex, and striatum but not the CA1 pyramidal neurons in hippocampus (Prüss et al., 2005). We therefore believe that the light-activated potassium current described here most likely arises from temperature-dependent modulation of inwardly rectifying potassium channels.

Light drives temperature shifts that alter neuronal activity and behavior

Our experiments indicate that light-driven temperature changes can markedly reduce firing rates of many types of neurons, and the magnitude of this effect is sufficient to affect behavior. With this in mind, we suggest that two essential experimental design considerations: minimize light power and duration, and ensure that control experiments rigorously account for potential off-target effects of light delivery (Yizhar et al., 2011, Gysbrechts et al., 2016). Experiments that include light-driven activation of opsins should ideally be accompanied by two separate controls: opsin-free, in which light is delivered but no opsin is present; and light-free, in which the opsin is expressed but light is not delivered. Comparing results to both control conditions provides the best opportunity to identify off-target effects of light delivery or opsin expression. Importantly, the efficiency of optical fiber implants, the power and duration of light delivery, and the quality of the surgical preparation must be identical for all opsin-free control animals. Blinding of the experimenter to the identity of animals during surgical preparation and performance of experiments can help ensure the rigor of these procedures.

Several factors can help to minimize light delivery while preserving efficient and specific activation of opsins. First, close attention should be paid to opsin expression. Our experiments indicate that light-driven temperature changes can markedly reduce firing rates of MSNs *in vivo* and in acute slices. This opsin-independent modulation of neuronal circuit activity by light can cloud the interpretation of optogenetic or imaging experiments. We therefore propose three guidelines for avoiding this potentially major confound: (1) allow adequate time for opsin expression, in order to use the lowest light power and shortest duration of illumination possible for any experiment; (2) attend to the quality and rigor of opsin-independent (e.g. static fluorophore only) control experiments; and (3) consider the time-course of physiological responses to light delivery, because temperature-driven responses are expected to be an order of magnitude slower than optogenetically driven changes in activity. With respect to opsin expression, excitatory opsins such as channelrhodopsin-2 generally express well in mammalian systems within ~2 weeks, whereas inhibitory opsins such as eNpHR3.0 or eArchT can take as long as 6-8 weeks to develop significant photocurrents because of poorer membrane trafficking (Gradinaru et al., 2010). Any apparent physiological responses to light that occur before opsin expression is fully developed should clearly be treated with caution. The continuously growing toolbox of opsins with altered spectral sensitivity (Klapoetke et al., 2014, Lin et al., 2013, Chuong et al., 2014) or kinetics (Berndt et al., 2009) opens the door for use of lower light powers or longer wavelengths that generate less heating (Figure 2.S1E). New technologies, including tapered fibers, waveguides, and micro-LEDs that spread light more evenly across the tissue, support efficient and homogenous opsin activation across larger structures with reduced light power (Pisanello et al., 2017, Steude et al., 2016, Wu et al., 2013).

Careful consideration of the time-course of light-driven responses can help to differentiate opsin-driven effects from opsin-independent experimental artifacts. With regard to kinetics, the time-constants that describe optogenetic tools and neuronal membranes are on the

order of ones to tens of milliseconds. This is true for direct optogenetic excitation of neuronal populations (Kravitz et al., 2013, Pi et al., 2013), and for indirect synaptic disinhibition arising from optogenetic silencing of inhibitory neuronal populations (Mattis et al., 2012). By contrast, the time-constant for heating of neuronal tissue with light (Stujenske et al., 2015, Arias-Gil et al., 2016) is markedly slower (Figure 2.5B,C, 1.S1A-C). Physiological responses to light delivery that develop slowly, over hundreds of milliseconds or seconds should therefore be suspected of arising from local heating of tissue rather than a directly opsin-dependent physiological process. In these cases, we suggest that a higher bar ought to be met by the experimenter to describe a mechanism to reconcile the time-course of the optogenetic manipulation with the time-course of the physiological response and to establish the rigor of opsin-independent control experiments.

CONCLUDING REMARKS

The broader results of this study are two-fold. First, for the striatal community, this work represents firm experimental evidence that the net effect of FSI activity is the inhibition of surrounding MSNs. Understanding how FSIs may contribute to MSN activity patterns will allow the field to move forward and perform more detailed and sophisticated experiments examining this important microcircuit. Second, this study brings up a relevant light-related artifact that may influence both physiology and behavior. Here, we demonstrate how light power can reverse the direction of an optogenetic manipulation, and how it can directly drive behavior via a physiological change. As light is increasingly used in neuroscience for optical methods including stimulation experiments with optogenetics, as well as recording studies with various genetically encoded indicators, a firm understanding of safe light illumination protocols are vital to prevent the proliferation of artefactual results. In a brief survey of the literature, we have found a number of studies in slice electrophysiology, in vivo electrophysiology, and behavior that appear remarkably similar to the temperature dependent results we have produced here. The point of

this work is not to shame individual researchers, but to inform the scientific community of important caveats to some extremely important tools for modern neuroscience.

These results regarding light-induced heating of the brain also bring up additional questions that require further study. First, do these temperature mediated changes in physiology occur in brain regions we have not recorded from, and via mechanisms beyond the Kir channels? Second, given that body temperature often fluctuates with the circadian cycle, is there an effect of circadian cycle on microcircuit and overall brain function via temperature? For example, does our finding help to explain the physiological basis for phenomena such as febrile seizures? Third, how do changes in physiology scale with broader changes in temperature? We have only sampled a small temperature range, and it is possible that further increases or decreases in temperature could have different effects on neuronal physiology. Understanding these changes could help to understand what happens with more severe changes in brain temperature, such as in the setting of hypothermia.

MATERIALS AND METHODS:

Mice

60 adult mice on a C57BL/6 background, aged 45 to 250 days, and of both sexes were used in experiments. All animals were group housed and maintained on a 12/12 light dark cycle and fed ad libitum. N = 3 wild-type mice (2 female; 1 male; Jackson Stock #000664) were used for *in vivo* electrophysiology experiments. N = 4 wild-type mice (2 female; 2 male; Jackson Stock #000664) were used for *in vivo* temperature recording experiments. N = 29 wild-type mice (12 males; 17 females; Jackson Stock #000664) were used in slice electrophysiology experiments. N = 5 PV-2A-Cre mice (3 male, 2 female; Jackson Stock #012358) were used for eNpHR3.0-driven optogenetic suppression during in vivo electrophysiology experiments. N = 7 PV-Arbr-Cre (4 male, 3 female; Jackson Stock #017320) were used for eNpHR3.0-driven optogenetic suppression during in vivo electrophysiology experiments. . N = 12 wild-type mice (4 female; 8 male; Jackson Stock #000664) were used for open-field behavioral experiment.

Sample size for physiological recordings were determined based on previously published studies, and statistical significance was calculated using post hoc tests. Recordings were performed in a standardized way to minimize possibility for experimenter bias. Age and sex of mice was balanced across cohorts, and littermates were used for fluorophore control experiments.

Stereotactic surgery

All procedures were in accordance with protocols approved by the UCSF Institutional Animal Care and Use Committee. Experiments were carried out during the light cycle. All surgeries were carried out under aseptic conditions, while mice were anaesthetized with isoflurane (3% for induction, 0.5-1.5% for maintenance) in a manual stereotactic frame (Kopf). Buprenorphine HCl (0.1 mg/kg, intraperitoneal injection) and Ketoprofen (5mg/kg, subcutaneous injection), were used for postoperative analgesia.

Headbar implantation.

WT mice were prepared for *in vivo* awake head-fixed recordings by surgical implantation of a headbar. Animals were mounted onto the stereotax and anaesthesia was induced as described above. The overlying scalp was removed, and the skull was cleaned and exposed. A stainless steel headbar (eMachineShops, custom design) was then secured with a combination of dental adhesives (C&B Metabond, Parkell, Lang). After dental adhesive had set, the scalp was sutured closed around the implant and mice were allowed to recover for at least 7 days before head fixation or recordings. For experiments involving expression of viral constructs, craniectomies were made during the head bar surgery, and 1000 uL of virus was injected. Viruses used in this project include: AAV5-EF1α-DIO-eNpHR3.0-YFP and AAV5-EF1α-DIO-mCherry (UNC vector core). Following viral injection, craniectomies were sealed with dental cement.

Head-fixed *in vivo* electrophysiology recordings

At least three days prior to recording, animals were acclimated to a head fixation device, consisting of a custom 3-D printed cylindrical running wheel (custom design, Evan Feinberg). Animals were monitored for any signs of distress or discomfort, and were head fixed for progressively longer periods of time leading up to the recording session. The night before a recording session, animals were anesthetized and mounted on a stereotax as described above. Craniectomies were made above the targeted recording area in dorsal striatum (+1.0 AP, +/-2.0 ML) bilaterally and covered with silicone elastomer (Body Double). Animals were then allowed to recover overnight before recording.

All extracellular recordings were performed using the Trodes data acquisition system (Spike Gadgets), and a 32 channel silicon probe (Cambridge Neurotech, ASSY-37 DBC-2-2, 2 shank probe with parallel electrodes, 9 mm length, 250 mm inter-shank spacing, 16 sites per shank). A 200 mm, 0.39 NA optical fiber was attached for light delivery (Thorlabs FT200UMT,

flat cut, mounted 750 mm above electrode sites, tip centered between shanks). Laser light was generated by TTL control of a 532 nm DPSS laser (Shanghai Laser Co).

Animals were head-fixed and the craniectomy exposed. Masking lights, consisting of two bright green LEDs (Sparkfun COM-00105) were positioned at each side of the head (2 cm distance from mouse) and illuminated throughout the experiment. A bank of 36 bright white LEDs (Sparkfun COM-0053) was positioned 15 cm anterior and superior to the mouse head and illuminated throughout the experiment. Finally, aluminum blinding dividers were lowered into place along the side of the head to reduce the ability of the animal to detect the onset of optogenetic light stimulation from above. A ground wire was then placed near the craniectomy and the probe was coated with CM-DiI to facilitate post-hoc reconstruction of the electrode track (ThermoFisher V22888). The probe was lowered through the craniectomy under the control of a motorized micromanipulator (Siskiyou MX1641L) until electrodes were in striatum (minimum depth of 2 mm from brain surface). The probe was allowed to settle for at least 30 minutes before recording. The recording sites centered on the dorsal striatum at +1.0 AP, +/-2.0 ML, -2.5 DV from brain surface

Recordings were sampled at 30 kHz, band-pass filtered (300-6,000 Hz), and analyzed for spiking activity. Neighboring sites on electrode shanks were divided into tetrodes for spike detection and analysis. Single units were isolated manually using peak amplitude and principal components as variables, using the MatClust script provided by SpikeGadgets. Electrode tracts were reconstructed post hoc using DiI fluorescence to confirm recording location.

Three different stimulation protocols were used for reported in vivo electrophysiology experiments. For all experiments, light powers for the laser were measured at the fiber tip of the probe before and after recordings (Thorlabs PM-100D with S130C). For data shown in Figure 2.1, animals received a 2 second stimulation of 3 mW light, with a 6 second inter-stimulation interval. In each recording, light stimulation was repeated a minimum of 300 times. For data

shown in Figure 2.2, animals received 5 seconds of either 3 mW or 15 mW light, with a 15 second inter-stimulation interval. Light power was varied in interleaved 50 trial blocks. In each recording, 100 stimulations were made for each laser power. For data shown in Figure 2.3, animals received 2 seconds of either 3 mW or 15 mW light, with a 6 second inter-stimulation interval. In each recording, 100 repetitions of 3 mW light was delivered first, followed by 100 repetitions of 15 mW light.

Head-fixed *in vivo* temperature measurement

WT animals were prepared with headbar surgery as described above, with the addition of a 200 mm, 0.39 NA optical fiber (Thorlabs FT200UMT, flat cut) chronically implanted into the brain and affixed to the skull during headbar surgery. The optical fiber was implanted at -1.0 AP, 2.0 ML, -3.0 DV and angled at 30 degrees from vertical in the posterior direction, to ensure ~1 mm of distance between the fiber tip and the thermocouple. Craniectomy sites were marked at +1.0 AP, 2.0 ML for insertion of temperature probe.

Mice were allowed to recover for two weeks then acclimated to head fixation as described above. Following acclimation, a craniectomy was made over marked sites and animals were recorded from the following day. Temperature recordings were performed with an OMEGA DAQ acquisition system (model 2401) coupled to a T-type hypodermic thermocouple (MT 29/5, Physitemp). The thermocouple was coated in CM DiI (Thermofisher) to mark the tract and inserted acutely using micromanipulator. After allowing temperature to stabilize, temperature change in response to laser illumination was recorded. Each laser power was delivered 30 times, with 5 second pulse duration and 20 second interval between onset of laser pulses.

Acute slice physiology

Wild-type mice 8-24 weeks of age were euthanized with a lethal dose of ketamine and xylazine followed by transcardial perfusion with 8 mL of ice cold artificial corticospinal fluid (ACSF) containing (in mM): NaCl (79), KCl (2.3), $NaHCO_3$ (23), Sucrose (68), NaH_2PO_4 (1.1), $MgCl_2$ (6), D-Glucose (12), $CaCl_2$ (0.5). Coronal slices (250 µm thick) containing dorsal striatum, primary sensory cortex, or dorsal hippocampus were then prepared with a vibratome (Leica) in the same solution before incubation in 33°C ACSF containing (in mM): NaCl (125), $NaHCO_3$ (26), NaH_2PO_4 (1.25), KCl (2.5), $MgCl_2$ (1), $CaCl_2$ (2), and D-Glucose (12.5), continuously bubbled with 95/5% O_2/CO_2. After 30-60 minutes of recovery at 35° C, slices were kept at room temperature until recording. For recordings, slices were transferred to a chamber superfused with recording ACSF (4-6 mL min^{-1}) at 28°C.

Whole-cell current-clamp recordings were obtained with an internal solution containing (in mM): K-Gluconate (135), NaCl (10), $MgCl_2$ (2), EGTA (0.5), HEPES (10), Mg-ATP (2), Na-GTP (0.3). Spiking activity was driven by injection of current steps 3 sec in duration through the recording pipette with an inter-sweep interval of 10-60 sec. Injection amplitude was chosen to drive spiking that was maintained throughout the 3 sec current step (250-600 pA). On interleaved sweeps, green laser light (532 nm) was delivered through a 200 mm optical fiber placed 500-800 mm from the recorded neuron at a power of either 3 mW or 15 mW. Light pulses were 1 sec in duration, spanning the middle 1 sec of the 3 sec current step injection. To calculate group data for spike rate modulation by light, the spike rate for each neuron on Light On trials was normalized to the spike rate for the equivalent period on Light Off trials. Three separate periods were analyzed, “Pre” (0-1 sec), “Light” (1-2 sec), and “Post” (2-3 sec after start of current step). To identify cortical neuron cell types, each waveform was up-sampled 10-fold using a spline fitting function in MATLAB, before calculating an average spike waveform from that neuron. The spike width was calculated as the full-width-half-maximum value of the action

potential peak relative to the pre-spike baseline membrane potential. A clear bimodal distribution emerged to disginguish putative pyramidal neurons (width > 0.7 ms) from putative interneurons (width < 0.7 ms).

Whole-cell voltage-clamp recordings of light-activated currents were performed using the same potassium-based internal solution in a set of neurons that partially overlapped with the current-clamp recordings. For whole-cell voltage-clamp recordings with a cesium-based internal solution, the internal recording solution contained (in mM): $CsMeSO_3$ (135), NaCl (8), EGTA (0.5), HEPES (10), Mg-ATP (2), Na-GTP (0.3), and QX-314 (5). For all voltage-clamp recordings, MSNs were held at a resting potential of -85 mV between sweeps. Membrane potentials are not corrected for junction potential. On each sweep, the voltage was stepped to -50 mV for 3 sec, and the light pulse (1 sec in duration) was delivered for the middle 1 sec of the 3 sec voltage step. Inter-sweep interval was 10-20 sec. Current amplitude was measured across three separate time windows: “Pre” (0.75-1 sec), “Light” (1.75-2 sec), and “Post” (2.5-2.75 sec after start of voltage step). The light-induced current was calculated by subtracting the average current amplitude over the “Pre” and “Post” periods from the average current over the “Light” period. This average was calculated separately for “Light On” and “Light Off” sweeps, and the final light-induced current for each cell was determined by subtracting the “Light Off” value from the “Light On” value.

An equivalent protocol was used to calculate the I-V curve and rectification of the light-activated current. The MSN was held at a resting potential of -85 mV with a potassium-based internal recording solution, and the voltage was stepped to varying holding potentials over a range from -140 mV to -50 mV for 3 sec with the light pulse (1 sec in duration) delivered over the middle 1 sec of the 3 sec voltage step.

For $BaCl_2$ wash-in experiments, the inter-sweep interval was extended to 60 sec. Light-activated currents were recorded at a holding potential stepped to -50 mV with a potassium-

based internal as described above. Recordings were maintained for at least 5 minutes after break-in to ensure recording stability before introducing 250 mM $BaCl_2$ to the bath solution. Recordings were maintained for at least 15-20 min following the application of $BaCl_2$. Leak current was measured as the average current over 250 ms before onset of the light, and was subtracted from each trace to account for effects of $BaCl_2$ on leak or background conductance independent of its effect on the light-activated current.

Temperature control in acute slices

A custom-designed system was constructed to locally control temperature in acute slices. A short length of copper tubing was bent into a U-shape, and an additional copper extension was soldered to the end of the U to contact the slice. A peristaltic pump produced a recirculating flow while solenoids were used to gate the source of temperature-controlled water inside the copper tubing. Controlled warming of the tubing was accomplished by rapidly switching the flow from an in-line solution heater (Warner Instruments) to pass through the copper tubing using TTL-gated solenoids (NResearch) to rapidly switch fluid flow. Cooling was accomplished by rapidly switching the flow to a source that passed through a short ~15 cm length of coiled copper tubing inside an ice bath immediately prior to entering the tubing that was in contact with the slice.

Temperature calibration

Temperature measurements in slice were performed with the same temperature setup of an Omega DAQ box and T-type thermocouple. In the slice rig, the tip of the sensor was placed at the approximate location of the recording site relative to the fiber or copper tubing with the bath perfusion system operating as usual for acute slice recordings. Temperature change was measured during laser delivery or passage of hot, warm, or cold fluids through the copper tubing. Measurements for each power were repeated 30 times.

Open Field Behavior

WT animals were prepared with headbar surgery as described above, with the addition of bilateral 200 mm, 0.39 NA optical fibers (Thorlabs FT200UMT, flat cut) chronically implanted into the brain and affixed to the skull during headbar surgery. The optical fibers were implanted at Bregma +1.0 AP, 1.5 ML, -2.2 DV.

Mice were allowed to recover for two weeks then acclimated to human handling. The open field arena was a pair of 25 cm diameter circular arenas lit from below and the sides with bright white LED strip lighting, to minimize the visual salience of laser illumination. Video was recorded at 30 fps using an area scan camera (Basler acA1300-60gm). Laser illumination was generated via two 532 nm DPSS lasers (Shanghai Laser Co), via dual commutators (Doric FRJ_1x2i_FC-2FC). Power was tested at the end of the fiber patch cable at the beginning of each behavioral session, and between animals, and was corrected for the recorded efficiency of the implanted fibers for each animal. Mice were run two at a time, one in each behavioral arena.

Fifteen minutes before each behavioral session, animals received an IP injection of 3 mg/kg of amphetamine (d-amphetamine hemisulfate salt, Sigma-Aldrich A5880 in sterile saline). This limited habituation to the open field environment and ensured consistent locomotion throughout behavioral sessions (Figure 2.6G-J). At the start of each session, a fiber optic patch cable was attached unilaterally to one of the implanted optical fibers in dorsal striatum. The mouse was placed in the open field for 30 minutes, during which time the laser was illuminated in a 10 second on, 30 second off cycle. The optical fiber was moved to the opposite side and the behavior was repeated before returning the mouse to its home cage. Laser power was held constant for all sessions on each day.

Data analysis for *in vivo* physiology

Striatal units were separated based on waveform into putative medium spiny neurons (MSNs), putative fast-spiking interneurons (FSIs), and putative cholinergic interneurons (ChATs). Putative ChATs were selected based on regularity of firing (maximum ISI coefficient of variation = 1.1), and excluded from further analysis. Putative FSIs were selected based on narrow waveform (maximum width = 0.4 ms) and excluded from further analysis. Putative MSNs were selected based on wide waveform (minimum width = 0.5 ms). Units with intermediate waveform width (0.4-0.5 ms) were classified as unknown, and also excluded from further analysis.

Modulation index was calculated as:

$$\text{Modulation Index} = (R1 - R2) / (R1 + R2)$$

R1 represents average firing rate during the entire duration of laser illumination. R2 represents the average firing rate for an equal period of time immediately before laser illumination. For data presented in Figure 2.1, R1 and R2 were averaged over 2 seconds, while for data presented in Figure 2.2, R1 and R2 were averaged over 5 seconds. Data presented in Figure 2.3 is analyzed differently due to the excitatory sensory artifact (Figure 2.3C, bottom left). Following published protocol (Lee et al., 2017), R1 and R2 were averaged over one second windows, with R1 representing the firing rate from one to two seconds after laser onset, and R2 representing the firing rate from two to one second before laser onset. In this way, the modulation index was not contaminated by the excitatory artifact.

Data analysis for open field behavior

Open field videos were first split into individual videos of each area using FFMPEG. Following this, they were processed using DeepLabCut, a machine learning package that can perform tracking of animal features. Data in this paper was analyzed using a network trained on

200 frames of recorded animal behavior that was run for 1 million training iterations. The network was trained to detect the tip of the nose, the base of each ear, and the base of the tail. The output of DeepLabCut is a series of x and y coordinates of each detected feature. We then extracted the mean position of the two ears by averaging the x and y coordinates of the ears, which we used as the center point of the mouse.

In order to determine total locomotion, we detected the change in position of the central point of the mouse across the entire session, and summed it by session. In order to determine change in mouse speed at laser onset, we extracted speed traces of the mouse center point aligned to laser onset. To determine the direction of the mouse, we generated a vector from the tail base to the center point. We then calculated the change in the direction of the mouse for every laser trial. To determine the rotations of the mouse, we wrote custom MATLAB code (MATHWORKS) that counted 90 degree rotations whenever a mouse changed its direction in one direction for 90 degrees. If the animal turned in the other direction for more than 45 degrees, then rotation tracking was reset for the new direction. Rotation times were defined as the frame in which the animal completed 90 degrees of rotation. Rotational analysis was performed blinded to the side of laser illumination. From these rotations, we then calculated rotational bias in ipsilateral or contralateral direction during the analysis time periods by the formula:

$$\text{Rotational Bias} = (CR - IR) / (CR + IR)$$

CR represents contralateral rotations, IR represents ipsilateral rotations.

Histology

Animals were euthanized with a lethal dose of ketamine and xylazine (400 mg ketamine plus 20 mg xylazine per kilogram of body weight, i.p.) and transcardially perfused with PBS, followed by 4% paraformaldehyde (PFA). Following perfusion, brains were transferred into 4%

PFA for 16 - 24 h and then moved to a 30% sucrose solution in PBS for 2 - 3 d (all at 4°C). Brains were then frozen and cut into 30 µm coronal sections with a sliding microtome (Leica Microsystems, model SM2000R) equipped with a freezing stage (Physitemp) and mounted on slides. Slides were blocked for 1 hour in 10% Normal Donkey Serum (NDS) in 0.5% PBST then incubated overnight in primary antibody (1:500 chicken anti-YFP, Aves Labs Inc, GFP-1020; and 1:500 rabbit anti-parvalbumin, Swant Inc., PV 27), 3% NDS in 0.5% PBST. The following day, they were washed 3 times for 10 minutes each in 0.5% PBST and incubated for 1 hour in secondary antibody (1:1000 donkey anti-chicken 488, Jackson Immunoresearch 703-545-155; and 1:1000 donkey anti-rabbit 647, Invitrogen, A-31573), 3% NDS in 0.5% PBST and 1:2000 DAPI. After this, slides were washed for 10 minutes in 0.5% PBST and 2 more 10 min periods with 1:1 PBS. Slides were then washed with 0.05% lithium carbonate and alcohol, rinsed with diH2O. Sections were coated with Cytoseal 60 and a coverslip was placed on top. Slides were imaged on a slide microscope and images processed manually using Fiji.

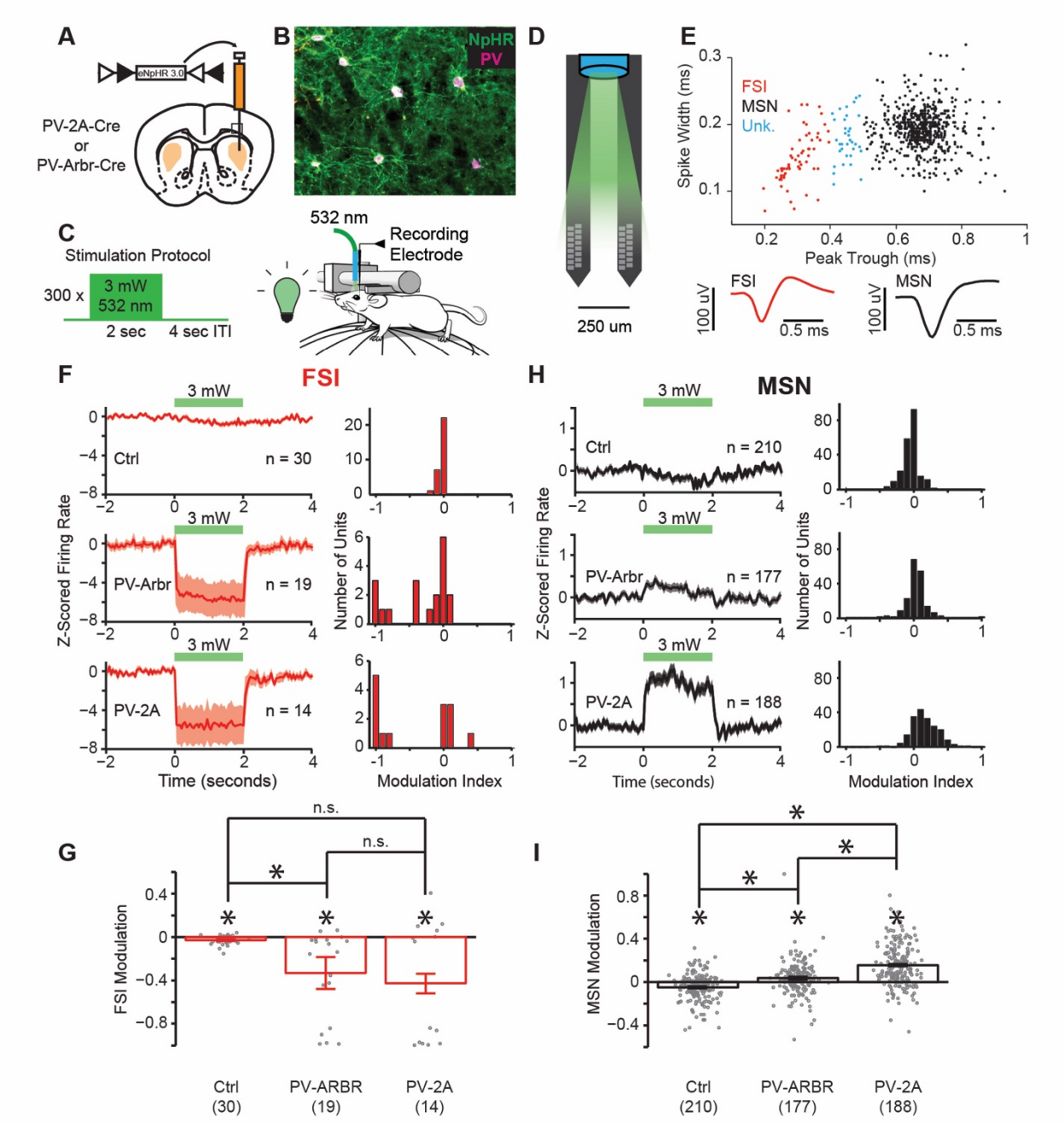


Figure 2. 1 Optogenetic Inhibition of Striatal PV+ Interneurons Produces Disinhibition of MSNs in Two PV-Cre Lines.

A, Viral injection: AAV-eNpHR3.0 was bilaterally injected into dorsal striatum in PV-2A-cre or PV-Arbr-cre lines.

B, Selective expression of eNpHR3.0 (green) by PV+ (purple) cells in dorsal striatum.

C, Laser stimulation and recording protocol. Animals are head fixed on a 1-D treadmill, and masked from laser light with physical barriers and masking lights (lightbulb).

D, Opto-electrode, containing two shanks with 16 electrodes each and a single 200mm core optical fiber. Scale bar, 250 mm.

E, Scatter plot single units based on peak-trough separation and spike width. Putative FSIs in red, putative MSNs in black. Unknown cells in blue. Bottom: example waveforms for putative FSI and MSN.

F, Effects of light on FSIs. Left: Mean z-scored firing rates $\pm$ s.e.m. from FSIs from fluorophore control animals, PV-Arbr-cre eNpHR3.0, and PV-2A-cre eNpHR3.0 expressing animals. N = 4 control, 3 PV-Arbr-cre, 3 PV-2A-cre mice. Right: Modulation indices for single units, see methods for calculation.

G, Mean changes $\pm$ s.e.m. in modulation index for three groups. Control and PV-Arbr-cre median value significantly different from zero (signed rank test, $p = 7.16 \times 10^{-4}$ and 0.0015 respectively). Control and PV-Arbr-cre significantly different from each other (rank sum test, p = 0.0134). PV-2A-cre median value not significantly different from zero or control (signed rank test, p = 0.0676, rank sum test, p = 0.3577).

H, Effects of light on MSNs. Left: Mean z-scored firing rates $\pm$ s.e.m. from MSNs from fluorophore control animals, PV-Arbr-cre eNpHR3.0, and PV-2A-cre eNpHR3.0 expressing animals. Right: Modulation indices for single units.

I, Mean changes + s.e.m. in modulation index for three groups. All groups median value significantly different from zero (signed rank test, $p = 1.8 \times 10^{-10}$, 5.03×10^{-5}, and 3.42×10^{-20} respectively). PV-Arbr-cre and PV-2A-cre median value significantly different from Control (rank sum test, $p = 8.25 \times 10^{-13}$ and 1.02×10^{-30}). PV-Arbr-cre and PV-2A-cre median values significantly different from each other (rank sum test, $p = 5.52 \times 10^{-11}$). All error bars s.e.m., * $P < 0.05$ ** $P < 0.01$ *** $P < 0.001$

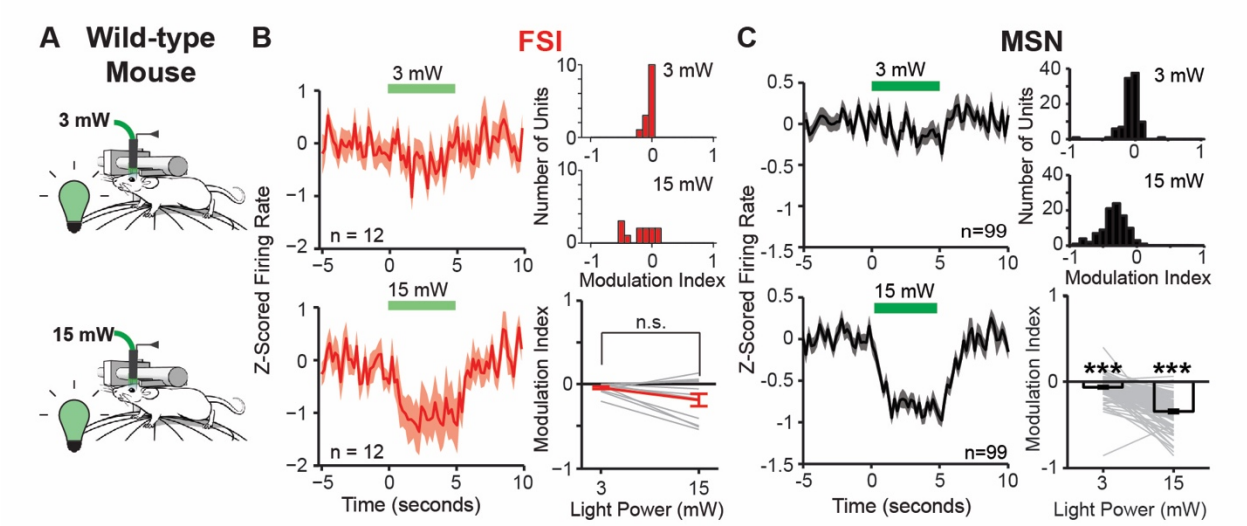


Figure 2. 2 Laser Light Alone is Sufficient to Induce Suppression of Neuronal Firing Rates In-Vivo Without Opsin Expression.

A, Schematic of recording setup. In each recording, the animal was presented with 3 mW and 15 mW light. Recordings were performed under masking lights (lightbulb). N = 3 WT mice.

B, Effects of laser light on FSIs (n = 12). Left: Averaged z-scored firing rates ± s.e.m. of FSIs during 3 mW (top) and 15 mW (bottom) light stimulation. Right Top: Histograms of modulation indices of FSIs for 3 mW and 15 mW light. Right Bottom: Individual and mean values ± s.e.m. for modulation indices for FSIs. Median values for 3 and 15 mW were not significantly different (signed rank test, p = 0.0771). Median values were significantly different from zero (signed rank test, p = 0.0049 and 0.0269 respectively).

C, Effect of laser light on MSNs (n = 99). Left: averaged z-scored firing rates ± s.e.m. of MSNs during 3 mW (top) and 15 mW (bottom) light stimulation. Right Top: histograms of modulation indices for MSNs. Right Bottom: Individual and mean values ± s.e.m. for modulation indices for MSNs. Median values for 3 and 15 mW were significantly different (signed rank test, $p = 1.88 \times 10^{-11}$). Median values were both significantly different from zero (signed rank test, $p = 8.98 \times 10^{-5}$ and 1.23×10^{-12} respectively). All error bars s.e.m., * P < 0.05 ** P < 0.01 *** P < 0.001

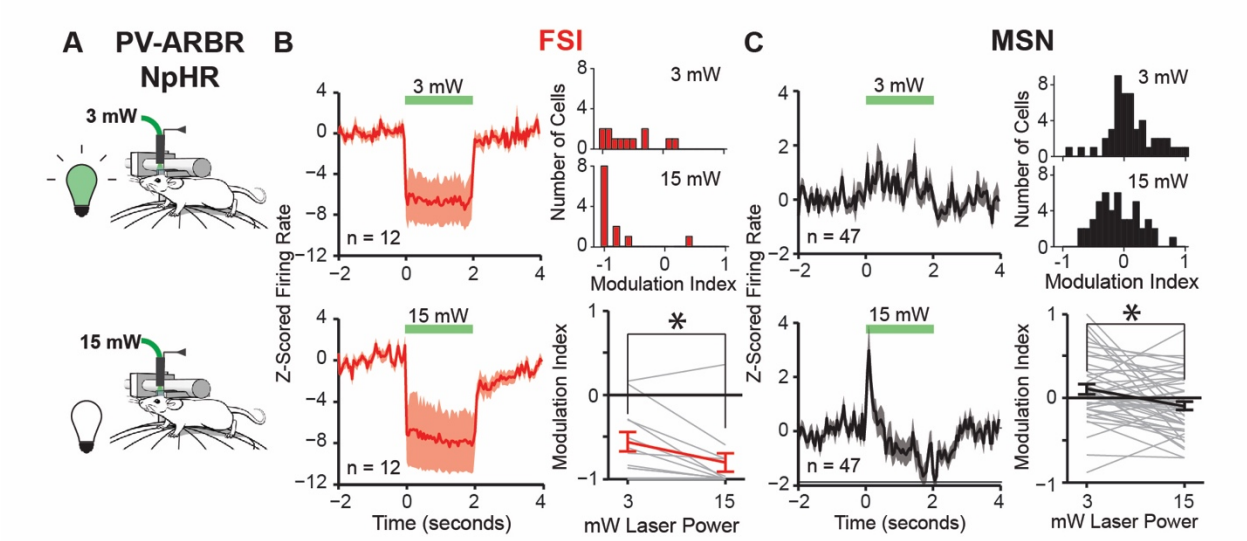


Figure 2. 3 Opsin-Independent Suppression of MSNs by 15 mW of Light Overcomes Disinhibition Arising from Optogenetic Silencing of PV+ Interneurons.

A, Schematic of recording setup. In each recording, PV-Arbr-cre eNpHR3.0 expressing animal was presented with both 3 mW (with masking lights) and 15 mW light (without masking lights). N = 2 animals.

B, Effect of laser light on FSIs (n = 12). Left: Averaged z-scored firing rates ± s.e.m. of FSIs during 3 mW (top) and 15 mW (bottom) light stimulation. Right Top: Histograms of modulation indices of FSIs for 3 mW and 15 mW light. Due to excitatory light response (Fig 3C, bottom left), modulation index excluded the first second of laser stimulation (see methods). Right Bottom: Individual and mean values ± s.e.m. for modulation indices for FSIs. Median values for 3 and 15 mW were significantly different (signed rank test, $p = 0.0137$). Median values were significantly different from zero (signed rank test, $p = 0.00244$ and 9.77×10^{-4} respectively).

C, Effect of laser light on MSNs (n = 47). Left: averaged z-scored firing rates ± s.e.m. of MSNs during 3 mW (top) and 15 mW (bottom) light stimulation. Right Top: histograms of modulation indices for MSNs. Right Bottom: Individual and mean values ± s.e.m. for modulation indices for MSNs. Median values for 3 and 15 mW were significantly different (signed rank test, $p = 0.0024$). Median values were not significantly different from zero (signed rank test, $p = 0.111$ and 0.0625, respectively). All error bars s.e.m., * $P < 0.05$ ** $P < 0.01$ *** $P < 0.001$

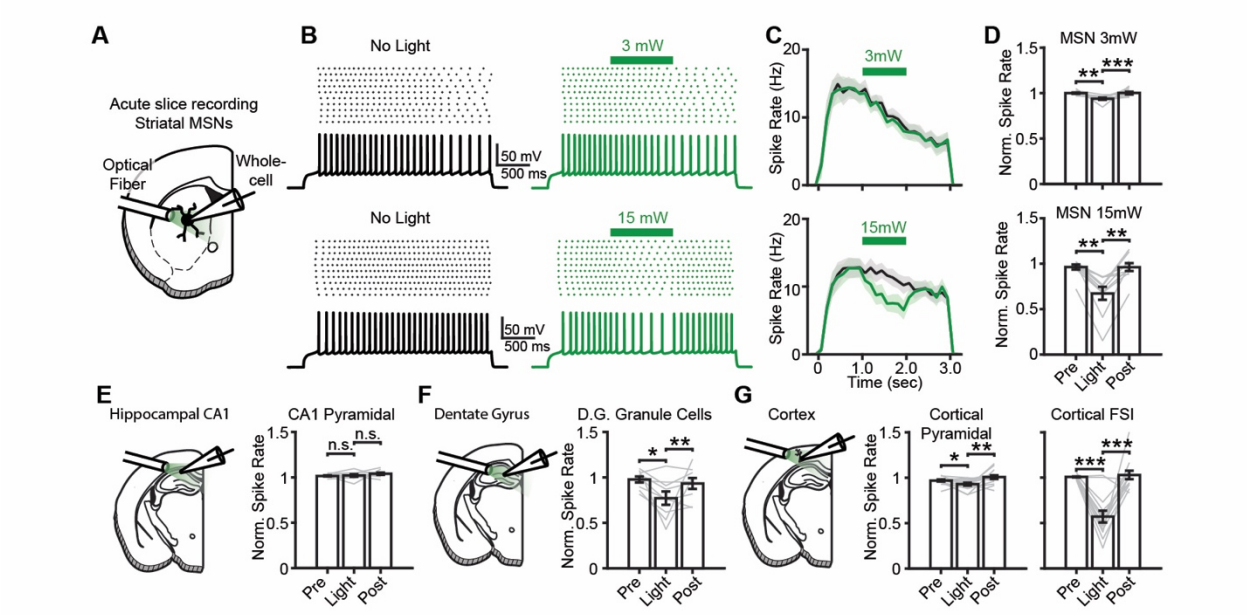


Figure 2. 4 Light delivery suppresses MSN activity *in vivo* and in acute slices.

A, Configuration for whole-cell recordings with light delivery through an optical fiber in acute slices.

B, Exemplar current-clamp recordings with spiking elicited by current injection (3 sec) through the recording electrode in the absence (left) or presence (right) of light delivery through the optical fiber. Light at 532 nm was delivered in a continuous 1 sec pulse. The power was either 3 mW (top) or 15 mW (bottom).

C,D, Group data show modest suppression of spiking by 3 mW and stronger suppression by 15 mW of light delivery in acute slices. Dark line is average, shaded area is +/- s.e.m with light on (green) or light off (black). N=2 mice, n=10 cells, P=0.002 and P=0.010 for 3 mW; N=2 mice, n=11 cells, P=0.002 and P=0.010 for 15 mW.

E-G, Firing rates are unaffected in CA1 pyramidal neurons (N=6 mice; n=10 cells; P=0.375 and P=0.432) and modestly suppressed by 15 mW light delivery in DG Granule cells (N=5 mice; n=9 cells; P=0.012 and P=0.098), and cortical L5 pyramidal neurons (N=5 mice; n=15 cells; P=0.026 and P=0.008). Stronger suppression was found in cortical L5 fast-spiking interneurons (N=8 mice; n=13 cells; P=0.001 and P=0.001), identified by narrow action potential spike width. All error bars are s.e.m. Signed rank test, * P<0.05, ** P<0.01, *** P<0.001.

=

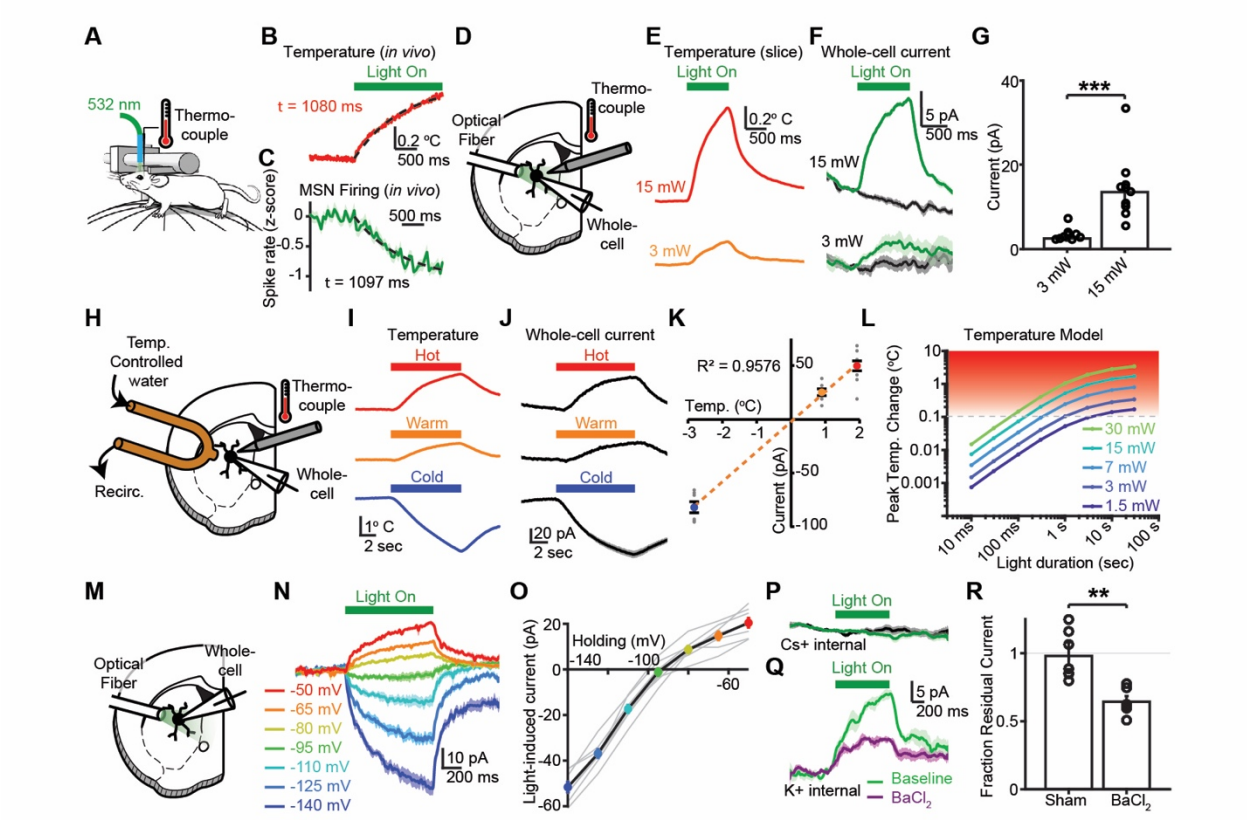


Figure 2. 5 Light-induced heating increases an inwardly-rectifying potassium conductance in MSNs.

A, Configuration for head-fixed thermocouple temperature measurements with light delivery *in vivo*.

B, Time-course of temperature increase *in vivo* fit to a single exponential matches closely with

C, time-course of decrease in MSN firing. Data reproduced from Figure 2D in response to 532 nm light at 15 mW. Dark line is mean, shaded area is +/- s.e.m. N=3 mice; n=99 MSNs.

D, Configuration for whole-cell recordings and temperature measurements in acute slices with light delivery through an optical fiber. Temperature measurements and whole-cell recordings were performed in separate experiments.

E, Exemplar light-driven temperature increase in an acute slice in response to 15 mW (top) or 3 mW (bottom) of light at 532 nm.

F, Exemplar voltage-clamp recordings depicting light-evoked currents in MSNs held at -50 mV. Light delivered at either 3 mW (top) or 15 mW (bottom). Recordings performed with potassium-based internal solution. Dark line is average, shaded area is +/- s.e.m with light on (green) or light off (black). N=2 mice; n=9 cells for 3 mW, n=10 cells for 15 mW.

G, Group data from experiment in panel F. Rank sum test, $P=4.33*10^{-5}$.

H, Configuration for acute slice whole-cell recordings from MSNs with custom-built local temperature modulation by water flow through a short length of copper tubing.

I, Thermocouple measurements of temperature changes in acute slices using the system in Panel H.

J, Temperature-induced currents in wild-type MSNs, recorded in voltage-clamp using a potassium-based internal solution.

K, Linear relationship between temperature change and current amplitude in MSNs. N=2 mice, n=7 cells for -2.82 °C; N=2 mice, n=7 cells for +0.89 °C; N=2 mice, n=10 cells for +1.92 °C.

L, Simulated temperature increase 750 mm from the tip of a 200 mm predicted by a previously published computer model for 532 nm light as a function of light power and pulse length[1].

M, Recording configuration for acute slice whole-cell recordings with light delivery through a 200 mm optical fiber.

N, Exemplar light-activated currents recorded under voltage-clamp at different holding potentials using a potassium-based internal solution. N=2 mice; n=8 cells.

O, Voltage sensitivity of light-activated currents. Same data as panel N.

P, Exemplar light-activated currents recorded under voltage-clamp in a wild-type MSN held at -50 mV with a cesium-based internal recording solution with light off (black) or light on (green). N=2 mice, n=10 cells.

Q, Exemplar light-activated current recorded under voltage-clamp in a wild-type MSN with a potassium-based internal recording solution before (green) and after (purple) bath application of 250 mM $BaCl_2$ (bottom). N=2 mice, n=7 cells sham; N=2 mice, n=6 cells $BaCl_2$.

R, Group data showing sensitivity of light-activated potassium conductance to extracellular $BaCl_2$ application. Same data as panel Q. Rank sum test, P=0.001. All error bars are s.e.m. ** P<0.01, *** P<0.001.

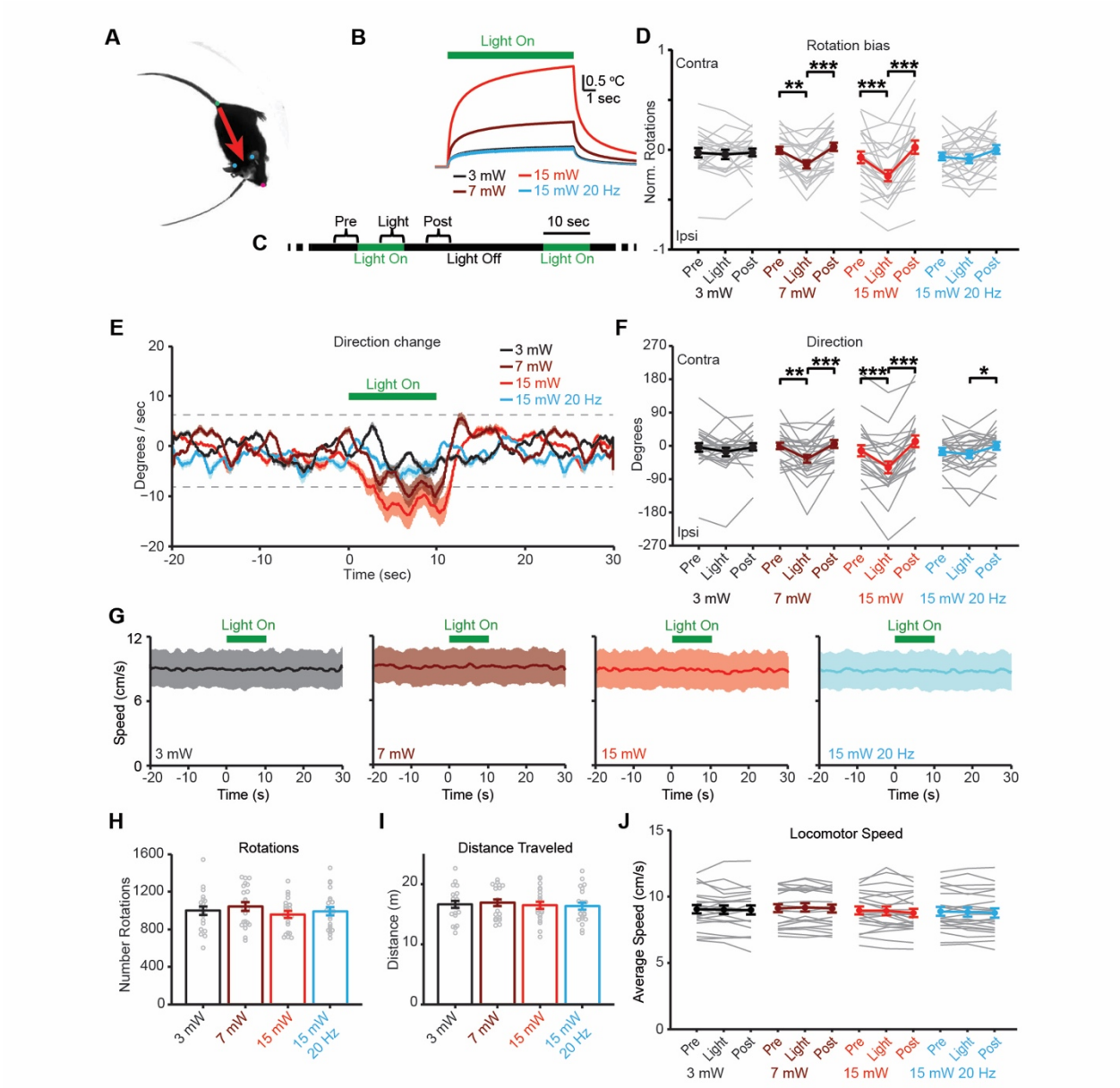


Figure 2. 6 Light illumination of dorsal striatum drives behavioral change.

A, Single video frame with labeled ear and tail positions derived from DeepLabCut position tracking. Red arrow indicates the direction vector of the mouse.

B, Simulated temperature change predicted by previously published computer model for 532 nm light 200 mm below the tip of 200 mm fiber. For pulsed light, peak power was 15 mW and pulse duration was 10 ms, oscillating at 20 Hz for a net duty cycle of 20%.

C, Light delivery paradigm for open field behavioral tests. Animals received 44 repetitions of unilateral illumination over a 30 min session with a 10 sec on, 30 sec off schedule. Pre, Light, and Post periods were used for analysis of behavior.

D, Mean change in rotational bias as in D. No significant change in rotational bias in 3 mW ($P = 0.37$ and $P = 0.66$) or 15 mW at 20 Hz ($P = 0.94$ and $P = 0.06$). Significant changes in bias for 7 mW ($P = 2.7 \times 10^{-3}$ and $P = 3.9 \times 10^{-4}$) and 15 mW ($P = 2.3 \times 10^{-4}$ and $P = 1.1 \times 10^{-5}$) by signed rank test.

E, Mean change in body direction aligned to light onset. Dotted lines represent 95% percentile bounds for baseline angle change (-20 to 0 seconds) for all sessions. N = 11 mice, 1 session per hemisphere per laser power condition.

F, Mean change in body direction over Pre, Light, and Post periods. N = 11 mice, 1 session per hemisphere per laser power condition. No significant change in body direction with 3 mW illumination (P = 0.06 and P = 0.13). Significant change with 7 mW (P = 0.002 and P = 2.6×10^{-4}) and 15 mW (P = 6.1×10^{-5} and P = 2.4×10^{-5}), and weak significant effect for 15 mW at 20 Hz (P = 0.67 and P = 0.03).

G, Instantaneous velocity across all laser conditions.

H,I, Mean total rotations (in all directions) and distance traveled for all laser conditions.

J, Mean change in velocity over Pre, Light, and Post periods. No significant changes. All error bars and shaded regions represent s.e.m. * P < 0.05 ** P < 0.01 *** P < 0.001.

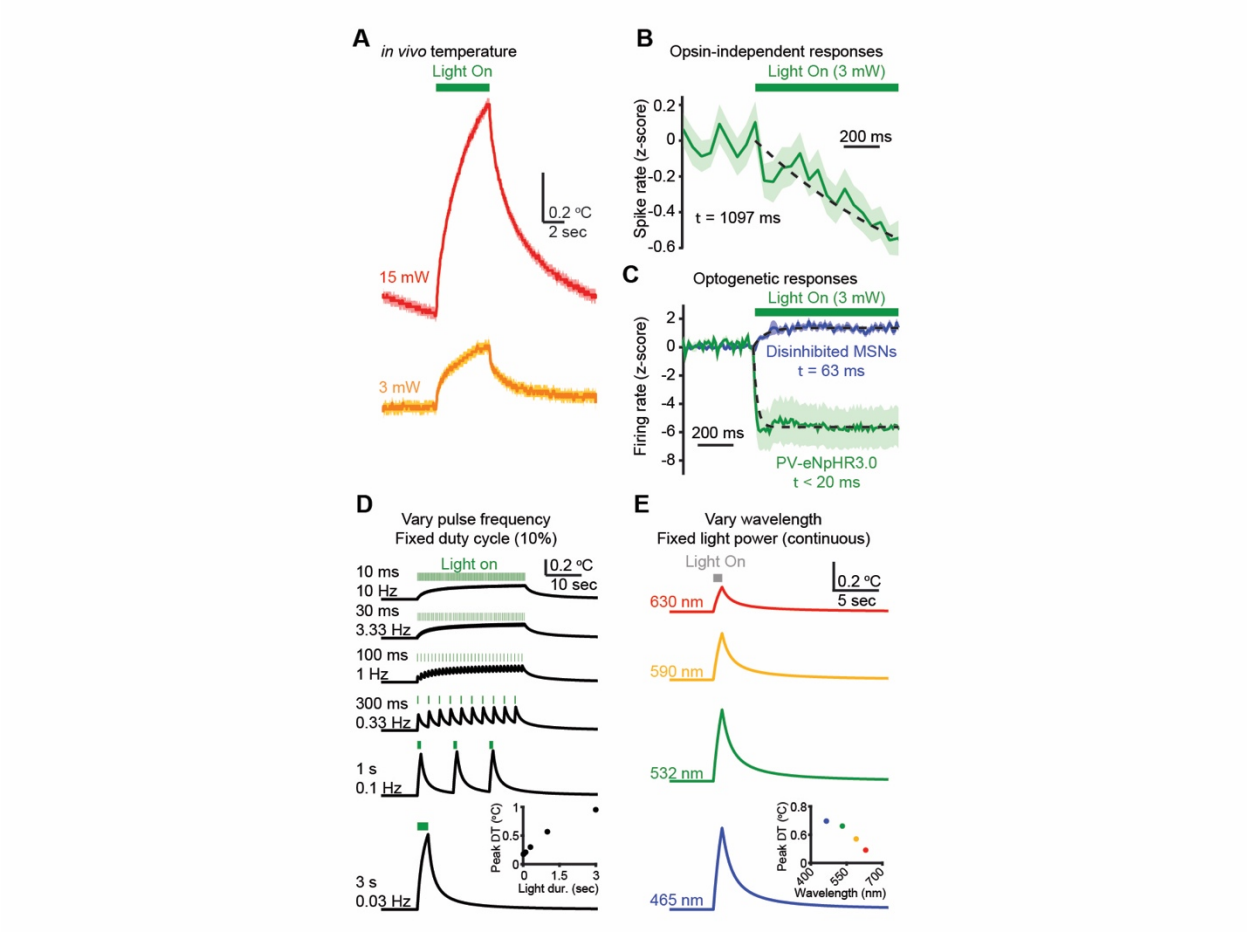


Figure 2.S 1 Time-course of light-driven temperature changes.

A, Full time-course of temperature changes measured using an acutely inserted thermocouple probe in dorsal striatum in response to light delivery at 3 mW (bottom) or 15 mW (top) N = 1 mouse. Data reproduced from Figure 2B.

B, Time-course of opsin-independent decrease in MSN firing. Data reproduced from Figure 2D in response to 532 nm light at 15 mW with time-scale adjusted to highlight contrast with optogenetic manipulation in Panel C.

C, Optogenetic silencing of FSIs (green) and disinhibition of neighboring MSNs (blue) occurs on a time-scale much shorter than light-driven temperature changes recorded in Panel B. N=5 PV-2A-cre mice; n=64 MSNs, n=16 FSIs.

D, Computer model simulations highlight the sensitivity of temperature changes to light pulse duration. Each trace represents equivalent light delivery (3 sec light over a 30 sec period = 10% duty cycle). Condensing this light into fewer pulses of longer duration each drives increased fluctuations in temperature. Simulation measured at 1 mm from the tip of a 200 mm optical fiber tip using 532 nm light at 15 mW.

E, Computer model of predicted temperature changes in response to 1 sec at 15 mW light delivered with commonly used wavelengths. Simulation measured 1mm from the tip of a 200 mm optical fiber. Shaded regions indicated mean +/- s.e.m.

CHAPTER 3

Investigating the role of FSIs in shaping MSN responses in auditory striatum

INTRODUCTION:

The work in Chapter 2 of this thesis should firmly establish that the gross effect of FSI activity in vivo is the suppression of MSN activity, and lay to rest the controversy generated by recent papers (Lee et al., 2017, Owen et al., 2018). While the finding of Chapter 2 is important in the understanding of the function of FSI-MSN microcircuit, this set of experiments fundamentally ignores the fact that FSIs and MSNs have very specific sensory and behavioral response selectivities (Gage et al., 2010, Yamamoto et al., 2012) that have important behavioral relevance (Kim and Hikosaka, 2013). Furthermore, it is theorized that alterations in MSN activity due to loss of FSIs is responsible for the behavioral phenotypes observed in disorders such as Tourettes (Kalanithi et al., 2005, Kataoka et al., 2013).

Given that FSIs clearly have some effect on MSN firing rates, and the selectivity of MSN activity is important for behavior, understanding how FSI activity may shape the selectivity of MSN responses is crucial to understanding FSIs may influence behavior. To do so, we must first understand the activity of both FSIs and MSNs. We can then examine how optogenetic inhibition of FSIs can influence the selectivity and magnitude of MSN activity.

Most studies examining the activity of FSIs and MSNs in vivo have focused on behavioral recordings in which activity is aligned to task relevant time points (Gage et al., 2010, Owen et al., 2018). While this body of work helps to shape our understanding of the activity within the striatum during behavior, it is difficult to fully resolve the response properties of MSNs

within a behavioral task, since the events provoking activity (movements and choices) are not under direct experimenter control. This makes it difficult to understand the receptive field of the recorded neurons (since the animal controls how much of the movement/behavior space it explores), requires careful tracking to implement properly, and is a challenging preparation in which to perform optogenetic manipulations (due to lack of experimenter control over behavior).

While there are relatively few studies investigating the precise function of feed-forward inhibition in striatum, FSIs appear in feed-forward circuits in a number of other brain regions, including the hippocampus and cortex. Work in these regions has elucidated a number of potential functions for feed-forward inhibition. These include control over spike timing (Wehr and Zador, 2003, Pouille and Scanziani, 2001), expansion of the dynamic range of a neuronal population (Pouille et al., 2009), gain control (Atallah et al., 2012), the sharpening of tuning (Wu et al., 2008), and maintaining oscillations in the brain (Sohal et al., 2009). Research on the effects of FSI activity on cortical pyramidal cells has also highlighted how it may provide divisive inhibition (Atallah et al., 2012), or subtractive inhibition (Lee et al., 2012, Phillips and Hasenstaub, 2016).

A key feature of these studies of feed-forward inhibition in other brain regions is the degree of control over the input, whether through choice of slice preparation (such as the hippocampus), or use of sensory regions in vivo, to afford the researcher some control over the inputs to the cell. Sensory regions also have the added benefit of helping to delineate the selectivity of the given neuron to sensory features of the stimulus, which may help us understand how the function of feed-forward inhibition could influence behaviorally relevant signals. Therefore, an alternative method to examine FSI modulation of MSNs is to take advantage of the sensory inputs to striatum, allowing the experimenter to probe a full range of stimuli, and present them with and without optogenetic intervention. Of the sensory inputs to the

striatum, visual, auditory, and somatosensory inputs have been characterized in the rodent model (Reig and Silberberg 2014, Bordi and LeDoux 1992), and all are possible candidates for investigating the role of FSIs in shaping MSN response selectivity.

Of these sensory modalities, the auditory responses of the striatum show the most promise for investigating specificity of neuronal responses. Auditory inputs from auditory thalamus and auditory cortex project to the most posterior aspect of the rodent striatum. These inputs are combined with inputs from motor cortex, higher order sensory cortices, and other sensory modalities, though there appears to be some topographic separation of different sensory inputs (Hintiryan et al., 2016, Hunnicutt et al. 2016).

Functional characterization of the auditory striatum reveals that it has frequency selective responses and likely plays a role in auditory guided behaviors. Recordings in the anesthetized rat have demonstrated that single units in the striatum exhibit consistent and frequency tuned responses to pure tones, similar to those observed in auditory thalamus or cortex (Bordi and Ledoux 1992). These findings have been confirmed in more recent studies in the awake rat and awake mouse (Znamenskiy and Zador 2013, Guo et al., 2018). Silencing of the auditory striatum completely abolishes the ability of mice to distinguish between tone frequencies, while preserving their understanding of overall task structure (Guo et al., 2018). Specific activation of subsets of cortical inputs to auditory striatum biases decisions in a manner dependent upon the best frequency of those cortical inputs (Znamenskiy and Zador 2013).

While these studies have clearly laid out that auditory striatum possesses selective sensory responses, and plays a key role in behavior, many open questions remain. Are both FSIs and MSNs responsive to auditory stimuli? If so, do their response properties vary? Finally, how does FSI activity modulate MSN tone responses? In this chapter, we will take advantage of the sensory control provided by the auditory striatum to take an in-depth look at the response

properties of neighboring FSIs and MSNs. We will then use optogenetic silencing of FSIs to examine how they contribute to MSN tone responses. We find that both FSIs and MSNs are responsive to pure tone and continuous stimuli. In response to pure tones, MSNs are more frequency selective than neighboring FSIs, which respond to a broader range of frequencies at lower amplitudes. In response to continuous stimuli, we observe that FSIs have narrower frequency tuning in their responses relative to their pure tone responses. In contrast, MSNs exhibit a diversity of differences between their continuous responses and pure tone responses. Finally, optogenetic suppression of FSIs produces a disinhibition of MSN tone responses, which results in a broadening of MSN frequency selectivity.

RESULTS:

MSNs and FSIs respond to pure tone auditory stimuli

To determine the responses of MSNs and FSIs to pure tone auditory stimuli, we performed acute, head-fixed extracellular recordings in the auditory striatum of awake mice. Mice were presented with 100 ms tone pips, and FSIs and MSNs were separated by waveform characteristics (Figure 3.1A-C). From our total dataset (N = 27 mice), we identified 770 putative MSNs and 102 putative FSIs. This ratio of MSNs to FSIs is largely consistent with published results (Gage et al., 2010, Lee et al., 2017, Owen et al., 2018) in other rodent studies in striatum.

As a population, both FSIs and MSNs responded to pure tone stimuli, and produced a variety of responses, including excitatory, inhibitory, and mixed (excitatory and inhibitory) responses. However, FSIs and MSNs differed in the proportion of responses they produced. While a similar proportion of FSIs and MSNs have negative or mixed responses to pure tones, a much larger proportion of FSIs (62%) are purely excited by tones when compared with MSNs

(34%). As a result, a very small proportion of FSIs are unresponsive to tones, while 39% of MSNs were unresponsive (Figure 3.2D).

In order to examine properties of FSI and MSN responses, we selected units with a minimum of five excitatory responses (see Methods), isolating a population of 147 MSNs and 56 FSIs. In these cells, we determined the threshold amplitude, width of frequency tuning (tuning width) at 70 dB SPL, best frequency, and response latency to best frequency (see methods for calculations, Figure 3.1E,F).

We found that a greater proportion of FSIs have lower threshold amplitudes than MSNs, though many neurons of both cell types had thresholds at the lowest measured amplitude. FSIs also exhibit broader tuning width at 70 dB (Figure 3.1E). Since many FSIs and MSNs have threshold amplitudes at or below 30dB, we further examined tuning width of these units. Here, we found that FSIs have a wider average tuning width than MSNs at every amplitude of tone presented (Figure 3.S1).

While FSIs and MSNs exhibit differences in threshold amplitude and tuning width, both populations have similar mean response latencies (Figure 3.1H). Notably, both FSIs and MSNs are capable of responding to pure tones with very rapid latencies (7-8 ms), similar to latencies seen in primary auditory cortex, and only slightly slower than responses in auditory thalamus (Anderson et al., 2011, Joachimsthaler et al., 2014). While the mean latency of FSIs and MSNs is not significantly different, FSIs and MSNs do appear to have a different distribution in latencies, such that a greater proportion of FSIs respond before 10 ms when compared with MSNs (Figure 3.S2A). This difference is also reflected in the normalized population PSTH, in which FSIs have a peak in firing rate that precedes the MSNs (Figure 3.S2B,C).

Finally, both FSIs and MSNs exhibit best frequencies across the range of tested frequencies, though there are fewer units representing higher frequencies.

MSNs and FSIs respond to continuous auditory stimuli

To measure the responses of MSNs and FSIs to continuous stimuli that more closely mimic natural sounds, we performed head-fixed awake recordings and presented a subset of animals (N = 17 mice, n = 506 MSNs, n = 65 FSIs) with pure tones followed by dynamic moving ripple (DMR) stimuli (Escabi and Schreiner 2002, Figure 3.2A). From the responses of the units to DMR stimuli, we were able to calculate spectrotemporal receptive fields (STRFs). STRFs can be averaged in the time dimension to produce tuning curves of positive and negative energy (Figure 3.2A, bottom right). Example STRFs for MSNs and FSIs are shown, and demonstrate the range of responses present in both cell types (Figure 3.2B,C).

Both MSNs and FSIs responded to the DMR, and displayed a diversity of responses to the DMR and pure tones. MSNs were predominantly unresponsive (34%), responsive only to the tone (35%), or responsive to both the tone and the DMR (27%). A small percentage of MSNs were responsive specifically to the DMR (4%). In contrast, FSIs were more or less split between being only responsive to the tone (42%) and responding to both the tone and DMR (55%) (Figure 3.2D).

In both pure tone and DMR stimuli, we can measure the frequency tuning and best frequency, and compare these values between the two stimuli. We examined these properties in a subset of cells that had significant positive responses to the pure tones and significant STRFs, isolating a population of 107 MSNs and 36 FSIs. First, we find that while DMR responsive FSIs are universally excited by the ripple stimulus (measured by modulation index), MSNs exhibit a range of responses, including both excitation and inhibition (Figure 3.2E). Second, we find that while the best frequency of FSIs or MSNs is largely preserved between pure tones and the

DMR, there are bidirectional differences in the breadth of frequency tuning (Figure 3.2F, G). While FSIs are more broadly tuned to pure tone stimuli, they almost universally respond to a narrower range of frequencies during DMR presentation. In contrast, while MSNs are more narrowly tuned to pure tones, they exhibit a range of changes to frequency tuning in their STRFs, including narrowing (like FSIs) and broadening. This difference remains even when we select only for units with a pure tone threshold amplitude of $\leq$ 30 dB SPL, suggesting it is not simply a result of differences in threshold amplitude (Figure 3.2H).

Responses to the DMR stimulus can also be used to derive the ripple transfer function (RTF), which is the output of a two-dimensional fourier transform of the STRF (Figure 3.3A). From the ripple transfer function, we can derive two values: the preferred temporal modulation frequency, and the preferred spectral modulation frequency (Figure 3.3B, C). These reflect the specificity of the individual units to temporal and spectral changes in the stimulus.

Examining individual units, we can see the RTFs of the example STRFs (Figure 3.2B, C), presented in the same order (Figure 3.3D, G). We can generate a population average RTF, which reflects the overall properties of FSIs and MSNs (Figure 3.3 E, H). Here, we observe that FSIs and MSNs generally prefer lower spectral modulation, but differ in their preferences for temporal modulation. While MSNs on average prefer temporal modulations around 10 Hz, FSIs tend to have a best frequency at lower rates of temporal modulation. However, a greater proportion of FSIs have good modulation at higher temporal modulations, above 20 Hz.

Examining single unit data, MSNs have a wider range of peak spectral and temporal modulations when compared with FSIs (Figure 3.3 F, I). These data in part reflect the findings of the population RTF, though it is notable very few FSI RTFs actually have best temporal modulation frequencies above 20 Hz.

Optogenetic Inhibition of FSIs in Auditory Striatum Disinhibits MSN Auditory responses

In order to determine how FSI activity helps to shape the responses of surrounding MSNs, we utilized optogenetic tools to silence FSI activity during tone presentations. Based on previous work in our lab (Chapter 1), we used the PV-2A-cre line to genetically target Halorhodopsin 3.0 (eNpHR 3.0) to striatal FSIs. Following 6-8 weeks of expression, we performed acute, head-fixed recordings in awake mice, and examined the responses of FSIs and MSNs with and without intracranial illumination (532 nm at 3 mW for 0.6 seconds, Figure 3.4 A, B).

Across a series of n = 14 recordings (N = 10 mice), we recorded from 45 putative FSIs and 345 putative MSNs. Across the two populations, we could examine the overall effect of inhibition by subtracting the mean tone only trial from the mean laser trial. For MSNs, we observe the rapid onset of moderate disinhibition with laser activation that remains constant over the pre-tone period. This disinhibition is larger during the tone period, before gradually reducing following the offset of the laser (Figure 3.4 C, top). For FSIs, we observe we maintain a rapid inhibition of FSI activity that remains constant through the pre-tone period. This inhibition is then larger during the tone period, and is relieved with the termination of the laser. This increase in inhibition during the tone period is due to floor effects of FSI inhibition, where the laser suppresses the baseline firing rate to zero (Figure 3.S3 A-C).

We can quantify the relationship of pre-tone disinhibition with tone disinhibition for MSNs (Figure 3.4 D). Here, we find that there is a strong positive correlation (correlation coefficient 0.56, P = 3.25 E-30) between disinhibition before the tone and disinhibition during the tone.

To examine the effects of disinhibition on population tuning properties, we first isolated units that were significantly modulated by laser and exhibited responses to pure tones (n = 21 FSIs, n = 57 MSNs). We can then generate average tuning curves, aligned to the best

frequency and normalized to the maximum response at 70 dB SPL without laser. If we do this, we find that FSIs are inhibited by the laser, while MSNs are disinhibited (Figure 3.4 E). We can also align to the individual best frequencies and normalize to the maximum response of the non-laser and laser trials respectively. If we do this, we find that the FSI tuning curve has become more narrow, while the MSN tuning curve has become more broad (Figure 3.4 F). Finally, we can examine the change in best frequency between non-laser and laser trials. Here we find that for both FSIs and MSNs, the majority of units do not experience significant change in best frequency (two sided signed rank test, P = 0.94 for FSIs, P = 0.98 for MSNs).

This analysis suggests that the effect of optogenetic inhibition of FSIs is to disinhibit MSN tone responses. To understand what is happening in the broader population of neurons that we recorded from, we selected for units that had significant tone responses (n = 28 FSIs, n = 102 MSNs) and examined how the optogenetic manipulation affected their tone responses. We did so using a linear framework borrowed from a recent publication in auditory cortex, in which researchers examined the effects of optogenetic suppression of different classes of interneurons (Phillips and Hasenstaub, 2016). We have reproduced their schematic for the organization of different types of effects of optogenetic stimulation (Figure 3.4 H). Analyzing the neurons from our dataset with this framework, we find that optogenetic inhibition of FSIs is successful in generating a significant change in 14/28 units (2 units were entirely suppressed, and therefore did not fit into this framework). MSNs, on the other hand, were largely disinhibited, either with multiplicative, additive, or a mixed disinhibition (Figure 3.4 I). This diversity of changes in MSN activity can be observed in single unit data (Figure 3.S3)

DISCUSSION:

FSIs respond to pure tones like surrounding MSNs, while exhibiting broader frequency tuning and lower thresholds for activation

In our experiments, we find that both FSIs and MSNs respond to a similar range of pure tone stimuli, though a greater proportion of FSIs are excited by pure tones (Figure 3.1 D). The greater proportion of FSIs responding to pure tones could be due to underlying differences in FSI/MSN responses to cortical input. These findings are consistent with the finding that FSIs respond to lower intensities of cortical electrical stimulation than surrounding MSNs (Mallet et al., 2005), and may be related with differences in organization of cortical inputs onto MSNs and FSIs (Kincaid et al., 1998, Bennett and Bolam, 1994). However, they might also reflect differences in the inputs to FSIs and MSNs, or the manner in which FSIs and MSNs sample inputs entering the striatum.

In our dataset, we also find that FSIs respond at lower threshold amplitudes and have broader frequency tuning at 70 dB (Figure 3.1 G). This difference in frequency holds true even for units selected for having the lowest threshold amplitudes from FSIs and MSNs (Figure 3.S1). These findings indicate that at a given amplitude, FSIs respond to a broader range of frequencies than surrounding MSNs. In this way, broader FSI inhibition could help to shape the responses of neighboring MSNs. While this difference is useful in understanding how responses of FSIs and MSNs may differ for a specific amplitude of stimulus, we cannot determine the shape of the tuning curve relative to the threshold amplitude, as we did not sample amplitudes low enough to resolve the threshold amplitude in most cases. This is a question that could be answered with further experiments using lower amplitude tones.

Finally, we observe that while FSIs and MSNs do not have a significant median difference in response latency (Figure 3.1 I), that a greater proportion of FSIs have < 10ms

latency responses than MSNs (Figure 3.S2). While these results do not exhibit the large differences in response latency that have been observed in some other feedforward circuits (Li et al., 2015), they are still largely consistent with the hypothesis that FSIs provide fast, feed-forward inhibition onto surrounding MSNs.

FSIs and MSNs respond to continuous auditory stimuli, but have divergent breadth of frequency tuning.

While pure tones pips are useful as a simple metric of auditory responses, they are a poor representation of the auditory complexity of natural sounds, which often include continuous sounds with simultaneous power in multiple frequency bands. One stimulus that more closely approximates natural sounds, while avoiding the statistical limitations of actual natural sounds is the dynamic moving ripple (DMR). In the DMR, energy in a wide range of frequency bands is dynamically modulated to produce complex auditory stimuli. The response properties of the unit can be measured by performing reverse correlation analysis of the spike train with the stimulus to generate a spectrotemporal receptive field (STRF). The values of the STRF represent the average stimulus preceding a spike.

Both FSIs and MSNs respond strongly to DMR stimuli, though again, a greater proportion of FSIs are responsive to the DMR (Figure 3.2 D). When DMR and pure tone responses are compared, we noticed striking differences between MSNs and FSIs. Among units that are positively modulated by both pure tones and have significant STRFs, nearly all FSIs have narrower frequency tuning width to the DMR, while many MSNs have broader frequency tuning to the DMR (Figure 3.2G, H). While it is not uncommon for the STRF to have a narrower frequency tuning than the pure tone receptive field (Christoph Schreiner, personal communication), it is unclear why some MSNs exhibit broader frequency tuning in the context of the DMR stimulus. This may be due in part to a number of MSNs exhibiting non-canonical (V-

shaped) frequency tuning to pure tones, which would influence the measurement of tuning width. Alternatively, this might suggest that there are temporal properties to the stimuli that are necessary for MSN spiking, and that these specific stimuli are poorly represented by pure tones. Possibly relating to this, we find that a small percentage of MSNs exhibit responses only to the DMR stimulus, and not to pure tones at all (Figure 3.2 D).

While FSI STRFs are relatively homogenous, MSNs exhibit a greater diversity of response fields, often with complex temporal and spectral structure. This is reflected in the differences in best temporal and spectral modulation frequencies, in which MSNs have a wider range of best modulation frequencies in both spectral and temporal axes (Figure 3.2 F, I). These data suggest that MSNs may be selective for more specific auditory stimuli than FSIs.

Optogenetic suppression of FSIs disinhibits MSN tone responses

Optogenetic suppression of FSIs in auditory striatum disinhibits the responses of MSNs to auditory stimuli in a variety of ways, including disinhibition that appears more additive (Figure 3.S3 D-F) or multiplicative (Figure 3.S3 G-I) in nature. These data, consistent with the data presented in Chapter 1, confirms that one *in vivo* function of FSI activity is the suppression of MSN activity.

Examining the effect of our optogenetic inhibition on MSNs and FSIs, we see that over units significantly modulated by the light, FSIs tone responses are inhibited, while MSN tone responses are disinhibited (Figure 3.4 E). To understand the contribution of different types of inhibition (divisive vs subtractive) and disinhibition (multiplicative vs additive), we can compare the the curves produced by different forms of normalization. In the first set of tuning curves (Figure 3.4 E), we normalize both laser and non-laser trials to the best frequency and peak response of the non-laser trials. This helps us understand the overall effect of the laser, which is to inhibit FSIs and disinhibit MSNs. We can then examine the second set of tuning curves, in

which laser and non-laser trials are aligned and normalized to their respective best frequencies and peak responses (Figure 3.4 F). Normalization is obtained by dividing by the peak value, so this manipulation should eliminate multiplicative/divisive changes to the tuning curve. Here, we see that the FSI laser tuning curve with laser remains more narrow than the normal tuning curve, and that the MSN laser tuning curve is slightly wider than the normal tuning curve. These data suggest that the effect of the optogenetic manipulation is not a purely divisive/multiplicative effect, but also has subtractive/additive components. Finally, we find that optogenetic manipulations have little effect on the preferred frequencies across both FSIs and MSNs.

Looking at these changes at the single unit level across the broader population of tone responsive FSIs and MSNs, we find that using a linear framework, we can detect a mix of additive and multiplicative effects of optogenetic suppression (Figure 3.4 I). These data might suggest that FSIs in striatum may play a range of roles, including scaling of MSN responses and providing subtractive inhibition. These findings differ from recent work in auditory cortex, in which suppression of FSIs was generally found to produce additive effects on pyramidal cell activity (Phillips and Hasenstaub, 2016). However, work in other cortical regions, such as the visual cortex, has also offered conflicting results, suggesting FSIs act to linearly scale responses (Atallah et al., 2012) or that they provide subtractive inhibition (Lee et al., 2012), indicating that our understanding of the circuit function of FSIs may remain incomplete.

Recent work has highlighted the experimental artifacts that can be produced with the use of excitatory optogenetic tools to investigate the circuit function of inhibitory interneurons (Phillips and Hasenstaub, 2016). Clearly, the use of inhibitory opsin avoids many of the pitfalls caused by spiking non-linearities. However, it is unclear whether the effect of the inhibitory opsin on the inhibitory interneurons may affect interpretation of their circuit function. In these experiments, while several FSIs were completely silenced, most maintained some degree of

tone responses. Does the subtractive/divisive nature of inhibition of FSIs affect whether the disinhibition of MSNs is seen as additive/multiplicative? This question requires further modeling and experimental work to determine.

CONCLUDING REMARKS

This study serves as an attempt to better understand how FSIs might contribute to the specificity of MSN responses. Here, we demonstrate that FSIs and MSNs have frequency selective responses and complex responses to continuous stimuli. Generally, we find that MSNs have more selective responses to auditory stimuli than neighboring FSIs. Optogenetic suppression of FSIs causes a disinhibition of MSNs that involves both additive and multiplicative effects.

As a preliminary study of the properties of FSI and MSN responses in auditory striatum, this work leaves many open questions. The first of these is whether FSIs and MSNs receive different sets of inputs. We noted a difference in the frequency selectivity and threshold amplitude between the two cell types, and it is possible that this is due to differences in input or the sampling of input. To understand this, one possible experiment would be to express ChR2 in input regions, and then patch pairs of FSIs and MSNs while illuminating different regions of the slice with a small dot of blue light. In this way, we might be able to deliver minimal stimulation to cortical inputs and determine whether FSIs and MSNs actually share common inputs, or if they are actually receiving different sets of inputs from similar regions.

Another question this study raises is the exact nature of inhibitory and excitatory input to MSNs. As we are only recording spiking data, we cannot observe subthreshold changes in the MSN membrane potential, and as such, do not know how the tuning curve generated from spiking responses relates to that of the actual excitatory input. Work done by Zador and colleagues suggests that there are plastic changes to the strength of excitatory inputs onto

MSNs following behavioral training (Xiong et al., 2015). Does each MSN sample very widely across frequencies, but only spike to a small subset? Or does each MSN actually sample a relatively narrow range of inputs? Understanding these subthreshold changes could help us understand the limits of behavioral plasticity in the striatum. This could be determined by in vivo whole cell recordings.

This study also provides an interesting setting to examining FSI-MSN cross correlograms. Previous studies have either failed to find any evidence of inhibition (Gage et al., 2010), or found them in very few pairs of FSIs-MSNs (Bakhurin et al., 2016). This would be especially interesting in the setting of the auditory striatum, in which sensory properties of the ostensibly connected units could be compared. We have performed cross correlogram analyses (data not shown), and have found significant interactions suggestive of monosynaptic inhibition. However, our dataset is dominated by periods of synchronous activity due to sensory stimuli, which both influences the cross correlogram and might influence the results of this type of analysis. Further work could examine possible interactions by incorporating longer baseline periods, using implanted electrodes to achieve stable long-term recordings, or use mild optogenetic stimulation of MSNs to artificially elevate their firing rate and make such interactions more obvious.

Finally, it would be interesting to understand if differences exist in tone responses between direct and indirect pathway MSNs. We attempted to study this difference through two methods. In the first, we used ChR2 to perform optogenetic identification during acute recordings. While we found a number of indirect pathway neurons responsive to tones, we were unable to do so with direct pathway neurons, as one mouse line (EY217) failed to adequately label the auditory striatum, and the other (EY262) labeled too many cortical inputs, resulting in ictal activity. These data suggest that there are potentially differences between the direct and

indirect pathway in tone responses. Our second approach utilized these mouse lines in combination with the genetically encoded calcium indicator GCaMP6m. Here, we found that the indirect pathway and one direct pathway line (EY262) produced consistent tone responses, while the other direct pathway line (EY217) failed to respond to tones. This data might suggest that both direct and indirect pathway neurons respond to pure tones, but this finding must be qualified with the caveat that the EY262 calcium activity we observed could be due to labeling of cortical inputs. Regardless of these methodological difficulties, the question of direct and indirect pathway responses to sounds remains an interesting one, and should be examined.

MATERIALS AND METHODS:

Mice: 37 adult mice on a C57BL/6 background, aged 58 to 177 days, and of both sexes were used in experiments. All animals were group housed and maintained on a 12/12 light dark cycle and fed ad libitum. N = 19 wild-type mice (9 female; 10 male; Jackson Stock #000664) and N = 8 PV-2A-Cre mice (2 female; 6 male; Jackson Stock #012358) expressing Halorhodopsin were used for *in vivo* electrophysiology experiments to examine responses to pure tones. N = 9 wild-type mice (4 female; 5 male; Jackson Stock #000664) and N = 7 PV-2A-Cre mice (2 female; 5 males; Jackson Stock #012358) expressing halorhodopsin were used for examining responses to pure tones and continuous stimuli. N = 10 PV-2A-Cre mice (6 female; 4 male; Jackson Stock #012358) expressing halorhodopsin were used for optogenetic experiments.

Sample size for physiological recordings were determined based on previously published studies, and statistical significance was calculated using post hoc tests. Recordings were performed in a standardized way to minimize possibility for experimenter bias. Age and sex of mice was balanced across cohorts, and littermates were used for fluorophore control experiments.

Stereotactic surgery

All procedures were in accordance with protocols approved by the UCSF Institutional Animal Care and Use Committee. Experiments were carried out during the light cycle. All surgeries were carried out under aseptic conditions, while mice were anaesthetized with isoflurane (3% for induction, 0.5-1.5% for maintenance) in a manual stereotactic frame (Kopf). Buprenorphine HCl (0.1 mg/kg, intraperitoneal injection) and Ketoprofen (5mg/kg, subcutaneous injection), were used for postoperative analgesia.

Headbar implantation.

WT mice were prepared for *in vivo* awake head-fixed recordings by surgical implantation of a headbar. Animals were mounted onto the stereotax and anaesthesia was induced as described above. The overlying scalp was removed, and the skull was cleaned and exposed. A stainless steel headbar (eMachineShops, custom design) was then secured with a combination of dental adhesives (C&B Metabond, Parkell, Lang). After dental adhesive had set, the scalp was sutured closed around the implant and mice were allowed to recover for at least 7 days before head fixation or recordings. For experiments involving expression of viral constructs, craniectomies were made during the head bar surgery, and 200 nL of virus was injected. Viruses used in this project include: AAV5-EF1α-DIO-eNpHR3.0-YFP (UNC vector core). Following viral injection, craniectomies were sealed with dental cement.

Head-fixed *in vivo* electrophysiology recordings

At least three days prior to recording, animals were acclimated to a head fixation device, consisting of a custom 3-D printed cylindrical running wheel (custom design, Evan Feinberg) mounted on an air table within a large sound attenuation booth. Animals were monitored for any signs of distress or discomfort, and were head fixed for progressively longer periods of time leading up to the recording session. The night before a recording session, animals were anesthetized and mounted on a stereotax as described above. Craniectomies were made above the targeted recording area in dorsal striatum (-1.7 AP, +3.5 ML from bregma) bilaterally and covered with silicone elastomer (Body Double). Animals were then allowed to recover overnight before recording.

All extracellular recordings were performed using the Trodes data acquisition system (Spike Gadgets), and a 64 channel silicon probe (Cambridge Neurotech, ASSY-77 H-2, 2 shank

probe with parallel electrodes, 8 mm length, 250 mm inter-shank spacing, 32 sites per shank). A 125 mm OD, 0.37 NA optical fiber was attached for light delivery in optogenetic experiments (Doric fibers 100/125 0.37, flat cut, mounted 150 um above nearest electrode site, laterally displaced by 300 um, tip centered between shanks). Laser light was generated by TTL control of a 532 nm DPSS laser (Shanghai Laser Co).

Animals were head-fixed and the craniectomy exposed. For optogenetic experiments, masking lights, consisting of bright green LEDs and a bank of bright white LEDs were activated for the duration of the recording. For non-optogenetic recordings, all lights were turned off inside the sound attenuation chamber during recordings. A ground wire was then placed near the craniectomy and the probe was coated with CM-DiI to facilitate post-hoc reconstruction of the electrode track (ThermoFisher V22888). The probe was lowered through the craniectomy under the control of a motorized micromanipulator (Siskiyou MX1641L) until electrodes were in striatum (minimum depth of 3 mm from brain surface). The probe was allowed to settle for at least 30 minutes before recording. The recording sites centered on the dorsal striatum at -1.7 AP, +3.5 ML, -3.2 DV from brain surface

Recordings were sampled at 30 kHz, band-pass filtered (300-6,000 Hz), and analyzed for spiking activity. Neighboring sites on electrode shanks were divided into tetrodes for spike detection and analysis. Single units were isolated manually using peak amplitude and principal components as variables, using the MatClust script provided by SpikeGadgets. Electrode tracts were reconstructed post hoc using DiI fluorescence to confirm recording location.

For tuning curve recordings, animals were presented with pure tones from a calibrated free-field electrostatic speaker (TDT ES-1 driven by TDT ED-1) mounted contralaterally from the recorded hemisphere, at the same elevation as the mouse head, and 45 degrees from the midline. Tones (100 ms, with 5 ms cosine on/off ramps) were synthesized in computer software

(MATLAB) and delivered to the speaker driver via a high sampling frequency audio card (Roland Quad Capture). Tones presented ranged from 4 kHz to 32 kHz spaced at 0.2 octaves (producing 16 different frequencies) at five amplitudes (10 dB steps, 30-70 dB SPL). A subset of experiments also involved presentation of white noise at five amplitudes, but white noise responses were not analyzed. Tones were spaced between 800-1200 ms, with an exponential distribution. Animals received 30-40 repetitions of each frequency/amplitude pair. Frequencies and amplitudes were selected pseudorandomly, such that the entire set of frequencies and amplitudes were presented before any single one would be repeated.

For recordings with presentations of tuning curves and dynamic moving ripple (DMR) stimuli, animals were first presented with 20 repetitions of the above mentioned tones, and following a brief pause, were presented with a single 10 minute DMR stimulus. Two DMR stimuli were used for the dataset, with N = 7 experiencing one DMR stimulus (400Hz to 64 kHz), and N = 10 experiencing the other DMR stimulus (4 kHz to 64 kHz). DMR stimuli had a maximum spectral modulation of 4 cycles/octave, and maximum temporal modulation of 40 Hz. maximum modulation depth of the spectrotemporal envelope was 40 dB. Within the shared frequency range, there was no appreciable difference between the datasets, so they were combined.

For optogenetic experiments, a number of protocols were used. The first (used in n = 3 recordings) used ¼ octave steps and white noise, across three amplitudes (10 dB steps, 50-70 dB SPL). The second (used in n = 4 recordings) used ⅕ octave steps and white noise, across three amplitudes (50-70 dB SPL). The final protocol used 3/5 octave steps, no white noise, across nine amplitudes (2.5 dB steps, 50-70 dB). The results of these experiments were combined by correcting for differences in frequency sampling in analysis of tuning width.

Separation of FSI and MSN single unit data:

Striatal units were separated based on waveform into putative medium spiny neurons (MSNs), putative fast-spiking interneurons (FSIs), and putative cholinergic interneurons (ChATs). Putative ChATs were selected based on regularity of firing (maximum ISI coefficient of variation = 1.1), and excluded from further analysis. Putative FSIs were selected based on narrow waveform (maximum width = 0.55 ms) while MSNs were selected based on wide waveforms (minimum width 0.6 ms). Units with intermediate waveforms were classified as unknown and excluded from further analysis.

Analysis of pure tone responses:

Units were classified as having positive, negative, or mixed responses (Figure 3.1D) based on significant positive, negative, or positive and negative deviations ($p < 0.01$, two-sided signed rank test performed on each bin) in their overall pure tone peristimulus time histogram (5 ms bins, averaged across all frequencies and amplitudes). To select for units with robust tone responses, only units with 5 significant responses ($p < 0.01$, calculated based on the significance of two sided signed-rank test of number of spikes during baseline period vs during tone period (100 ms)) were used for further analysis of tuning properties. Threshold amplitude was determined as the first amplitude for which a response with $p < 0.01$ by two sided signed rank test was detected. Tuning width was determined as the width in octaves at 70 dB SPL to reach 10% of the peak response value. The difference in width between FSIs and MSNs in maintained with other width cutoff percentages, including 25% and 50%. Response latency was calculated off the averaged PSTH to the best frequency and the two nearest frequencies at 70 dB and 60 dB SPL. These spikes were then binned at 0.5 ms, and smoothed over 5 ms. Latency was determined as the time from tone onset for the z-scored firing rate to exceed a value of 2 z scores. Best frequency was determined as the largest response at 70 dB SPL.

For analysis of tuning widths of units with amplitude thresholds ≤ 30 dB SPL, the same width analysis was performed for this subset of units at every amplitude level.

For further analysis of FSI and MSN latency, histograms of latencies for both unit types were converted to cumulative distribution plots. Normalized population PSTHs were developed by peak normalizing each individual unit PSTH, averaging across all units, and then peak normalizing the overall average PSTH.

Analysis of DMR responses:

Spike data was processed into spike trains with 1 ms bins, to match the downsampled DMR stimulus. STRFs were calculated by reverse correlation. Significance of individual pixels of the STRF were calculated by , and were thresholded at $p < 0.05$. Overall significance of STRFs was calculated by calculating the correlation between STRFs generated by splitting the true spike train, and the correlation of 1000 jittered spike trains and the original STRF. Units with correlation coefficients exceeding the 99th percentile of the jittered correlations were considered to be significant. To determine whether units were significantly modulated by tone, DMR, or both, any significant response (positive or negative) among pure tone stimuli were used. Firing modulation change (Figure 3.2E) was calculated by calculating the average firing rate across the DMR with the baseline firing rate during pure tone presentations. Modulation index was calculated as:

$$\text{Modulation Index} = (R1 - R2) / (R1 + R2)$$

R1 represents average firing rate during baseline periods of the pure tone presentations, and R2 represents the average firing rate over the entire DMR.

Best frequency of STRFs were calculated by taking the $p < 0.05$ significance thresholded STRF, removing negative values, and compressing the STRF along the time axis. Best frequency was the frequency value with the highest amplitude. Analysis for best frequency was restricted to 4 kHz to 32 kHz, even though DMR stimuli went beyond these bounds, so as to make for equal comparison with pure tone stimuli. Tuning width was calculated for both pure tone and STRF data as the half-max width, though the same result is generated with other width criteria.

RTFs were generated with a 2-D fast fourier transform of the STRF, after which the RTF was folded along the temporal axis. Temporal and spectral modulation plots were generated by averaging across either the spectral or temporal axes respectively. Peak spectral and temporal modulation was derived as the absolute maximum value of temporal and spectral modulation plots. Average RTFs were generated by normalizing the area of individual unit RTFs to 1, and then averaging across all units. This resulting average was then peak normalized to 1.

Analysis of Optogenetic Experiments:

Recordings from optogenetic experiments were analyzed collectively in Matlab. In order to determine the net change in PSTH between laser and non-laser trials, all FSIs and all MSNs were averaged to generate population PSTHs (in Hz) for laser and non-laser trials. Non-laser trials were then subtracted from laser trials to determine the magnitude and time-course of optogenetic inhibition over the pre-tone and tone periods.

To determine the relationship between change in firing rate for pre-tone and tone periods for MSNs, we calculated a modulation index (see above) for pre-tone and tone periods, and then plotted these together. The correlation coefficient was obtained by using the Matlab function corrcoef.

To determine the population tuning curves for FSIs and MSNs with and without laser, we first selected for units that were significantly modulated by light illumination, ignoring the direction of this change. We then selected for units among those that were tone responsive. Using this population, we then could align the tuning curves of individual units for non-laser and laser trials. In one set of tuning curves (Figure 3.4 E), we aligned to the best frequency found in the non-laser trials, and divided by the response to the best frequency to normalize the curves. In the second set of tuning curves (Figure 3.4 F), we aligned non-laser and laser responses to their respective best frequencies. Change in best frequency was calculated by comparing the non-laser and laser best frequencies.

To determine the changes to response properties at the single unit level, we selected for MSNs and FSIs that had greater than 5 significant tone responses (P = 0.05). For these units, we then used standardized major axis regression (Matlab function gmregress) in order to account for measurement variance in both the x and y axes. For this analysis, we used the baseline subtracted number of spikes per tone for all tones presented, which differs from the analysis (Phillips and Hasenstaub, 2016) from which this analysis was based. This was due to the fact that MSN responses are fairly sparse and limiting analysis to only the responses that achieved significance for both non-laser and laser trials effectively eliminated the entire dataset. For FSI responses, this restriction eliminated all FSIs that were strongly inhibited, as these had very few significant responses during laser trials.

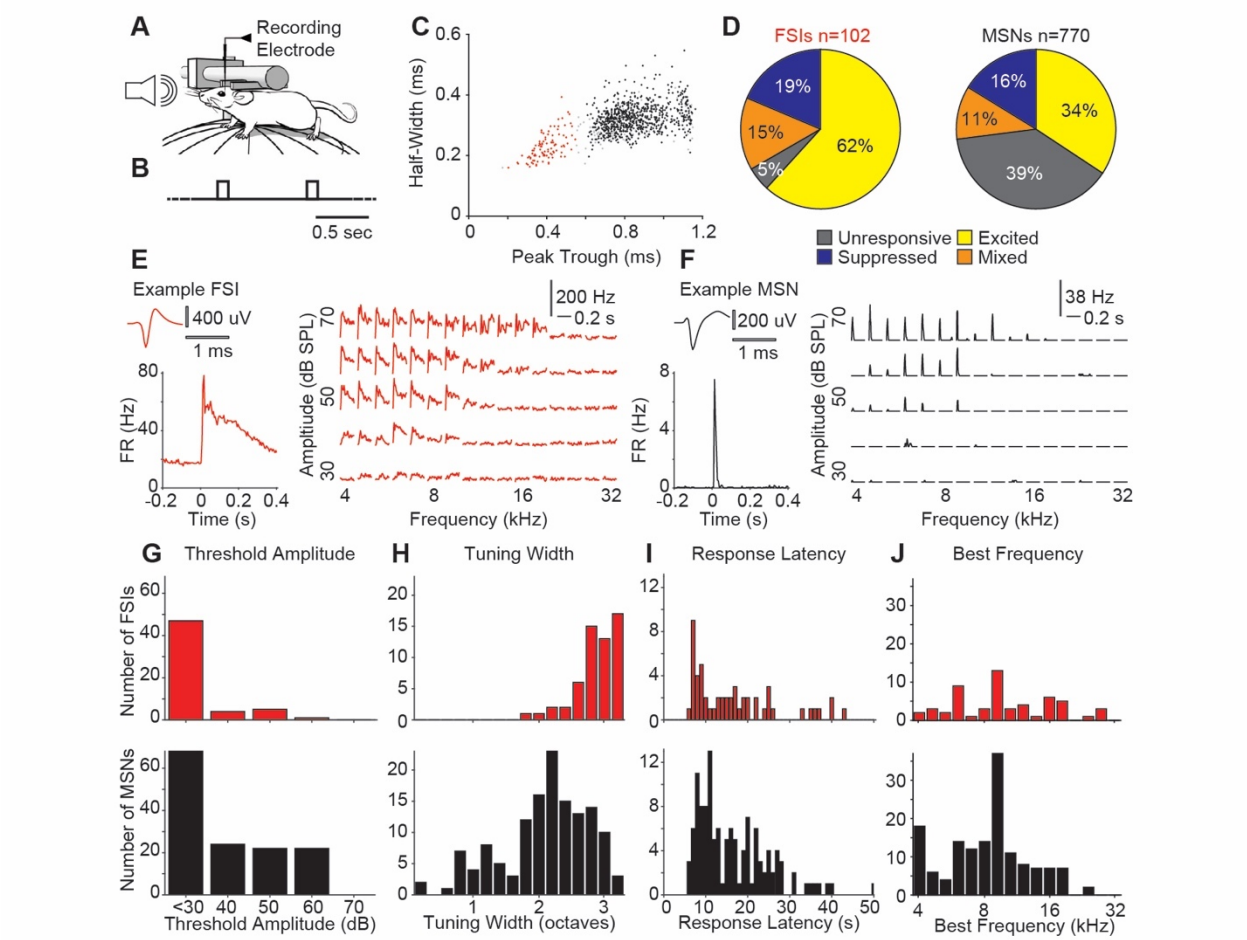


Figure 3. 1 FSIs and MSNs respond to pure tone stimuli.

A, B, Schematic of recording setup and tone presentation paradigm

C, Scatter plot showing separation of FSIs and MSNs by waveform. Units were separated by peak-trough time. FSIs in red, MSNs in black.

D, Proportion of FSIs and MSNs with different responses to tones.

E, Example data from an FSI. Top left, example waveform. Bottom left, overall PSTH in response to all frequencies and amplitudes. Right, PSTHs for each frequency and amplitude.

F, Example data from an MSN, from the same recording as E. Organized as above.

G, Distribution of threshold amplitudes for FSIs (in red) and MSNs (in black). Mean values are 33 (FSIs) and 39 (MSNs) dB SPL. Median value is significantly different (two-sided rank sum test, $P = 1.18 \times 10^{-4}$).

H, Distribution of tuning width, measured at 70 dB SPL, at 10% of peak value. FSIs in red, MSNs in black. Mean values are 2.9 (FSIs) and 2 (MSNs) octaves. Median value is significantly different (two-sided rank sum test, $P = 1.29 \times 10^{-14}$).

I, Distribution of latencies to best frequency, FSIs in red, MSNs in black. Mean values are 20.2 ms (FSIs) and 17.9 ms (MSNs). Median values not significantly different (two-sided rank sum test, P = 0.70).

J, Distribution of best frequencies, FSIs in red, MSNs in black.

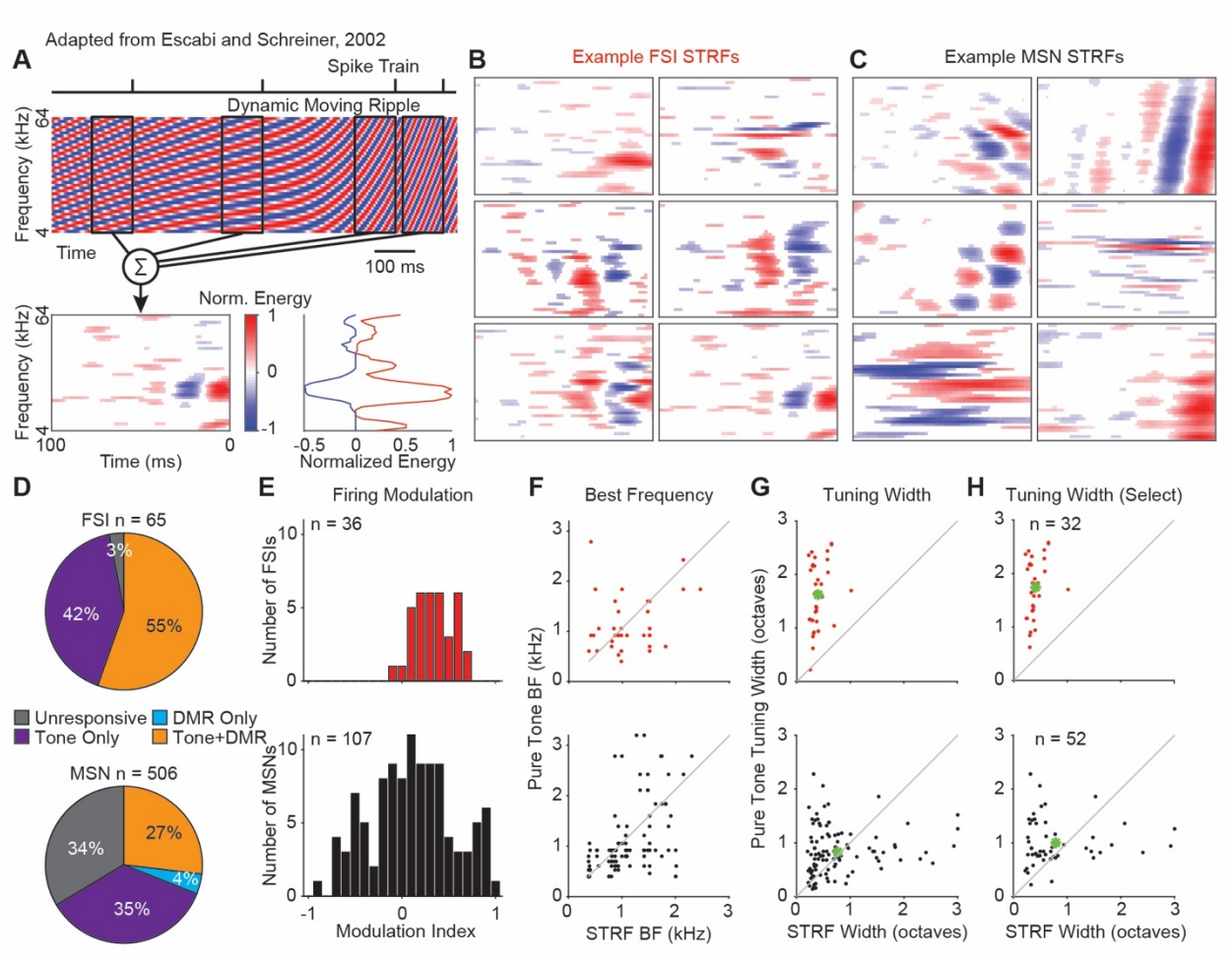


Figure 3. 2 FSIs and MSNs exhibit responses to dynamic moving ripple stimuli

A, Schematic reproduced from Escabi and Schreiner 2002 explaining how spectrotemporal receptive fields are derived from DMR stimulus and spike train. Top: periods of the stimulus before each spike are extracted and averaged using reverse correlation. This produces the STRF (bottom left). The STRF can be averaged across the time axis to generate frequency response curves of both positive and negative energy.

B, Example STRFs for FSIs.

C, Example STRFs for MSNs.

D, Proportions of FSIs and MSNs responding to pure tones, DMR, both, or neither

E, Modulation of firing rate averaged across DMR stimulus, relative to baseline rates during pure tone stimuli. FSIs in red, MSNs in black.

F, Best frequency for pure tone stimuli (x axis) and DMR stimulus (y axis), FSIs in red, MSNs in black.

G, Tuning width for pure tone stimuli (x axis) and DMR stimulus (y axis), FSIs in red, MSNs in black. Means represented by green dots.

H, Tuning width organized as above, selecting for FSIs and MSNs with threshold amplitudes at or below 30 dB SPL.

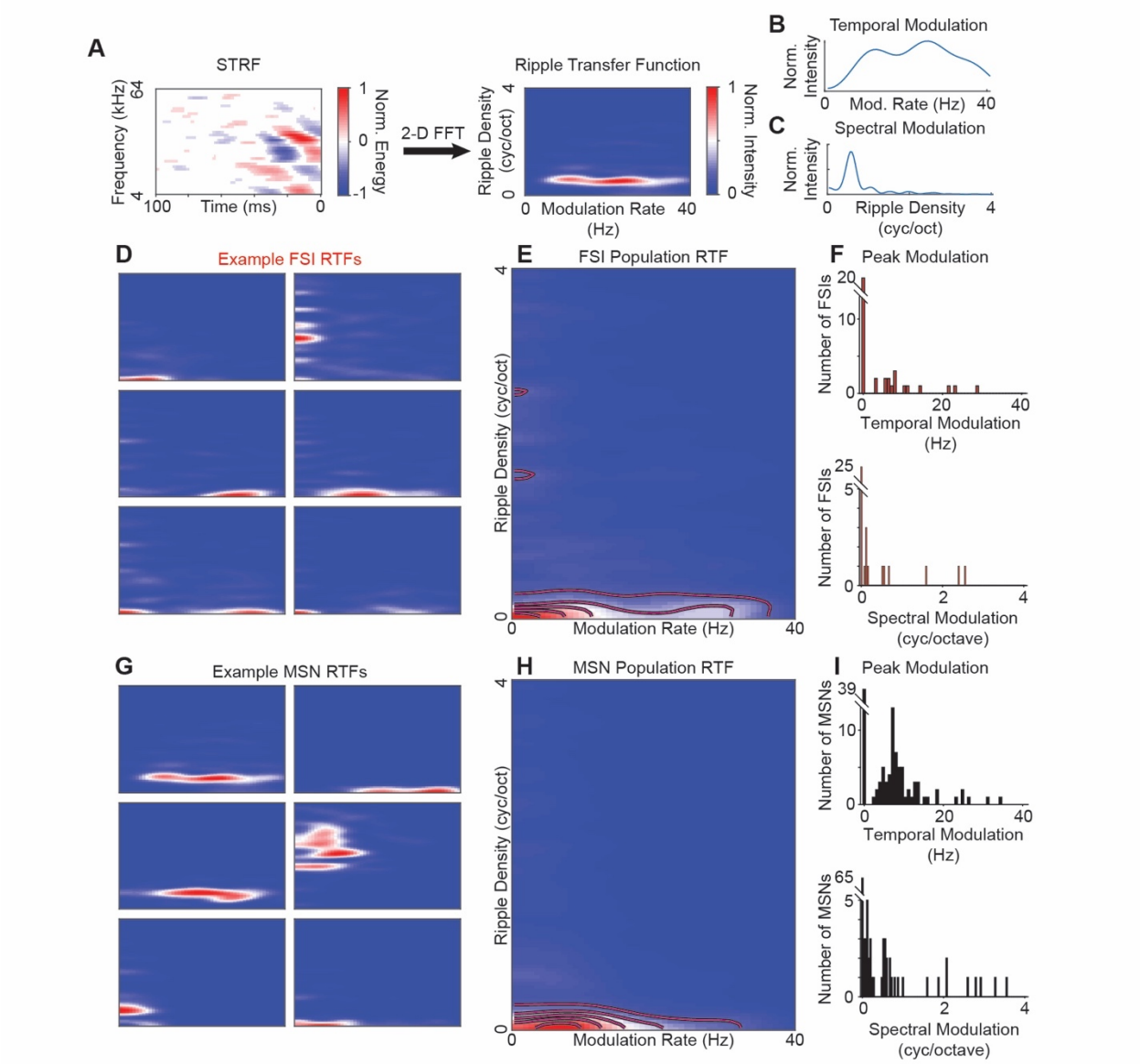


Figure 3. 3 Ripple transfer functions of FSIs and MSNs reveal differences in preferences for spectral and temporal modulation.

A, Schematic demonstrating the derivation of the RTF. The STRF (left) is processed via a 2-D fast fourier transform. The resulting output is then folded along the temporal axis to produce the RTF. Here, spectral modulation is represented along the y axis (ripple density) and temporal modulation along the x axis (modulation rate).

B, Temporal modulation derived from the RTF.

C, Spectral modulation derived from the RTF.

D, Example FSI RTFs, same units organized in same order as in Figure 3.2.

E, FSI population RTF. Intensity normalized to 1. Lines represent 20% contours.

F, FSI best temporal (top) and spectral (bottom) modulation rates.

G, Example MSN RTFs, same units organized in same order as in Figure 3.2.

H, MSN population RTF. As above in E.

I, MSN best temporal (top) and spectral (bottom) modulation rates.

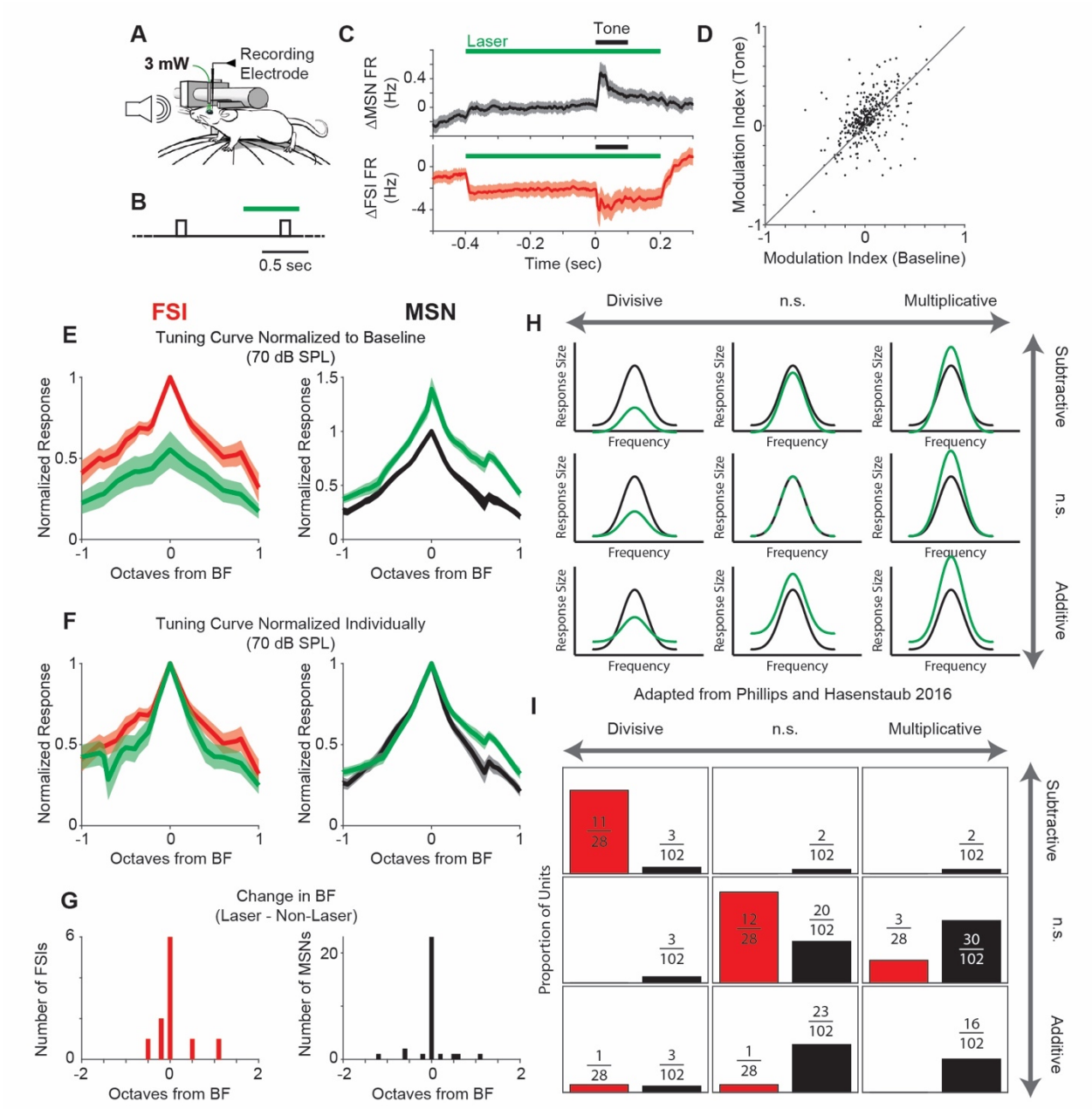


Figure 3. 4 Optogenetic inhibition of FSIs produces disinhibition of MSNs

A, B, Schematic showing experimental setup (A) and presentation of tones (B).

C, Population PSTHs showing difference between laser and non-laser trials for all MSNs (black) and FSIs (red).

D, Scatter plot of MSN modulation index before tone (x axis) and during tone (y axis).

E, Population tuning curves at 70 dB SPL for FSIs and MSNs, with laser responses in green and non-laser responses in red and black respectively. Normalized to the best frequency and peak response of the non-laser trials.

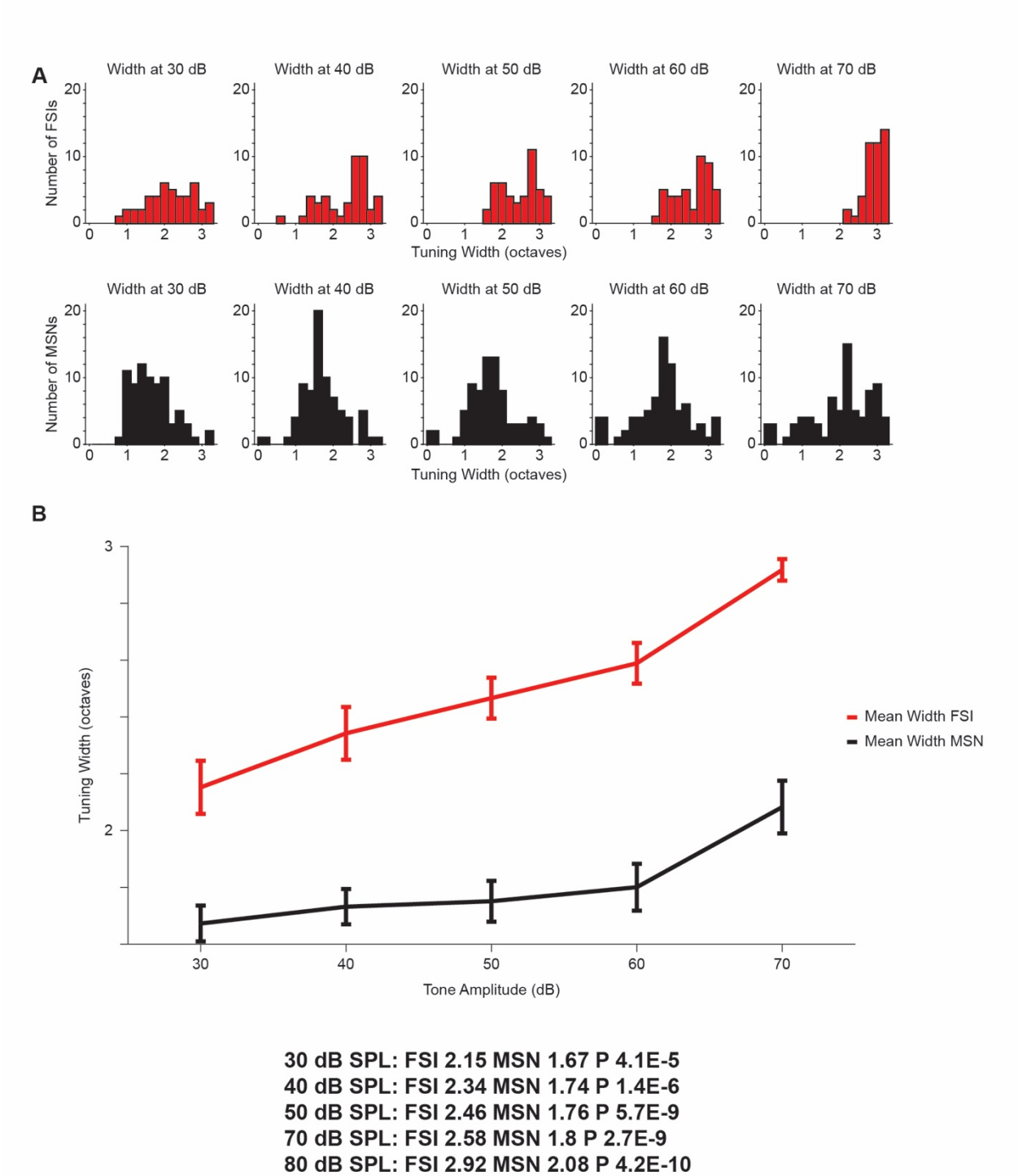
F, Population tuning curves at 70 dB SPL for FSIs and MSNs, organized as above. Here, tuning curves for laser and non-laser trials are normalized by their respective best frequencies and peak responses.

G, Change in best frequency for FSIs (red) and MSNs (black). No significant deviation from a zero-centered distribution for either (two-sided signed rank test, P = 0.94 (FSI) and P = 0.98 (MSN).

H, Schematic reproduced from Phillips and Hasenstaub 2016, showing how different types of linear transformations would appear in terms of shifts in the tuning curves.

I, Proportion of units displaying different types of changes, FSIs in red, MSNs in black.

All shaded areas represent s.e.m.



30 dB SPL: FSI 2.15 MSN 1.67 P 4.1E-5
40 dB SPL: FSI 2.34 MSN 1.74 P 1.4E-6
50 dB SPL: FSI 2.46 MSN 1.76 P 5.7E-9
70 dB SPL: FSI 2.58 MSN 1.8 P 2.7E-9
80 dB SPL: FSI 2.92 MSN 2.08 P 4.2E-10

Figure 3.S 1 Tuning widths across amplitudes for FSIs and MSNs with threshold amplitude equal to or less than 30 dB SPL

A, Distributions of widths for FSIs (n = 45, red) and MSNs (n = 76, black) at each decibel level.

B, Plot of mean +/- s.e.m. for tuning width of FSIs (red) and MSNs (black). Mean values and significance values (two-sided rank sum test) provided below.

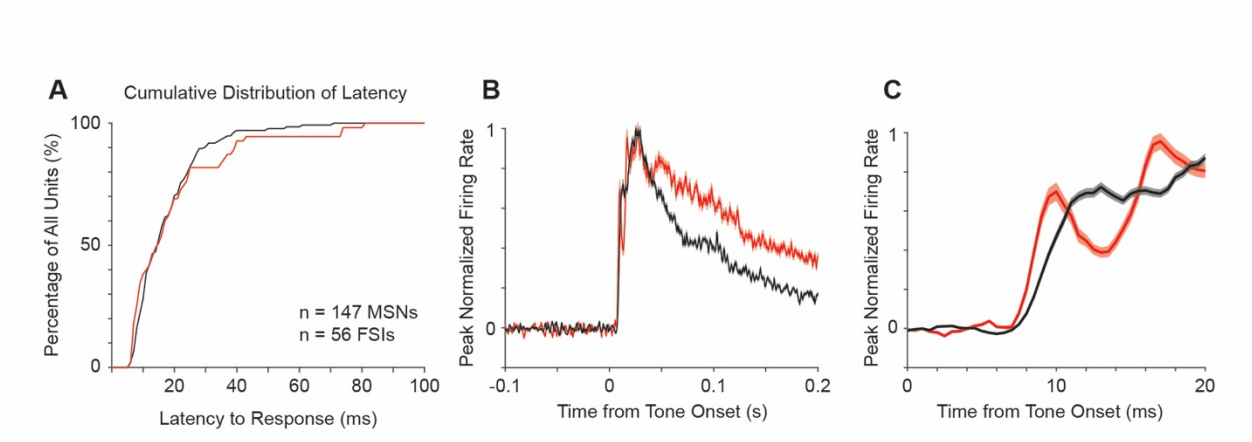


Figure 3.S 2 Differences in Latency for FSIs and MSNs.

A, Cumulative distribution plot for FSIs and MSNs.
B, Normalized population PSTH for FSIs (red) and MSNs (black).
C, Zoomed view of PSTH from B.
All shaded regions represent s.e.m.

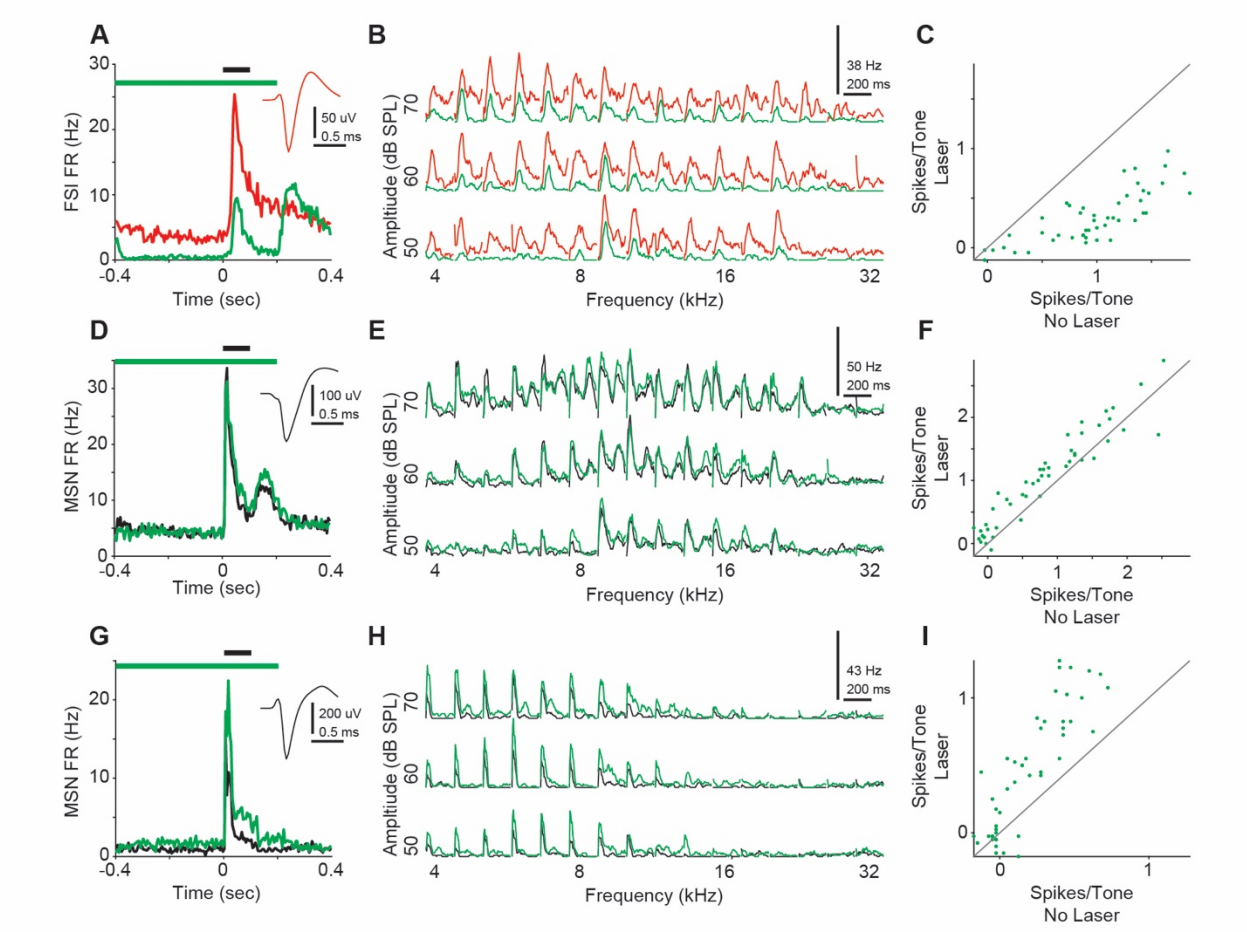


Figure 3.S 3 Examples of effects of optogenetic inhibition of FSIs.

A-C, Example data from a suppressed FSI. A, Waveform (top right) and average tone PSTH for non-laser (red) and laser (green) trials. B, Tuning curve showing PSTHs for tested frequencies and amplitudes. Non-laser trials in red, laser trials in green. C, Binned tone responses from non-laser trials (x axis) and laser trials (y axis). Unity line plotted in dark grey.
D-F, Example data from MSN exhibiting additive disinhibition. Organized as in A-C, except non-laser trials displayed in black.
G-I, Example data from MSN exhibiting multiplicative disinhibition. Organized as above.

REFERENCES:

Ait Ouares, K., Beurrier, C., Canepari, M., Laverne, G., & Kuczewski, N. (2019). Opto nongenetics inhibition of neuronal firing. *European Journal of Neuroscience*, *49*(1), 6–26. https://doi.org/10.1111/ejn.14251

Albin, R. L., Young, A. B., & Penney, J. B. (1989). The functional anatomy of basal ganglia disorders. *Trends in Neurosciences*, *12*(10), 366–375. Retrieved from http://www.ncbi.nlm.nih.gov/pubmed/2479133

Anderson, L. A., & Linden, J. F. (2011). Physiological differences between histologically defined subdivisions in the mouse auditory thalamus. *Hearing Research*, *274*(1–2), 48–60. https://doi.org/10.1016/j.heares.2010.12.016

Arias-Gil, G., Ohl, F. W., Takagaki, K., & Lippert, M. T. (2016). Measurement, modeling, and prediction of temperature rise due to optogenetic brain stimulation. *Neurophotonics*, *3*(4), 045007. https://doi.org/10.1117/1.NPh.3.4.045007

Atallah, B. V, Bruns, W., Carandini, M., & Scanziani, M. (2012). Parvalbumin-expressing interneurons linearly transform cortical responses to visual stimuli. *Neuron*, *73*(1), 159–170. https://doi.org/10.1016/j.neuron.2011.12.013

Atallah, B. V., Bruns, W., Carandini, M., & Scanziani, M. (2012). Parvalbumin-Expressing Interneurons Linearly Transform Cortical Responses to Visual Stimuli. *Neuron*, *73*(1), 159–170. https://doi.org/10.1016/j.neuron.2011.12.013

Atallah, B. V., Bruns, W., Carandini, M., & Scanziani, M. (2012). Parvalbumin-Expressing Interneurons Linearly Transform Cortical Responses to Visual Stimuli. *Neuron*, *73*(1), 159–170. https://doi.org/10.1016/j.neuron.2011.12.013

Bakhurin, K. I., Mac, V., Golshani, P., & Masmanidis, S. C. (2016). Temporal correlations among functionally specialized striatal neural ensembles in reward-conditioned mice. *Journal of Neurophysiology*, *115*(3), 1521–1532. https://doi.org/10.1152/jn.01037.2015

Bennett, B. D., & Bolam, J. P. (1994). Synaptic input and output of parvalbumin-immunoreactive neurons in the neostriatum of the rat. *Neuroscience*, *62*(3), 707–719. Retrieved from http://www.ncbi.nlm.nih.gov/pubmed/7870301

Berndt, A., Yizhar, O., Gunaydin, L. A., Hegemann, P., & Deisseroth, K. (2009). Bi-stable neural state switches. *Nature Neuroscience*, *12*(2), 229–234. https://doi.org/10.1038/nn.2247

BOLAM, J. P., HANLEY, J. J., BOOTH, P. A. C., & BEVAN, M. D. (2000). Synaptic organisation of the basal ganglia. *Journal of Anatomy*, *196*(4), 527–542. https://doi.org/10.1046/j.1469-7580.2000.19640527.x

Bordi, F., & LeDoux, J. (1992). Sensory tuning beyond the sensory system: an initial analysis of auditory response properties of neurons in the lateral amygdaloid nucleus and overlying areas of the striatum. *The Journal of Neuroscience : The Official Journal of the Society for Neuroscience*, *12*(7), 2493–2503.

Bordi, F., LeDoux, J., Clugnet, M. C., & Pavlides, C. (1993). Single-unit activity in the lateral nucleus of the amygdala and overlying areas of the striatum in freely behaving rats: rates, discharge patterns, and responses to acoustic stimuli. *Behavioral Neuroscience*, *107*(5), 757–769. https://doi.org/10.1037/0735-7044.107.5.757

Brelidze, T. I., Niu, X., & Magleby, K. L. (2003). A ring of eight conserved negatively charged amino acids doubles the conductance of BK channels and prevents inward rectification. *Proceedings of the National Academy of Sciences of the United States of America*, *100*(15), 9017–9022. https://doi.org/10.1073/pnas.1532257100

Burguière, E., Monteiro, P., Feng, G., & Graybiel, A. M. (2013). Optogenetic stimulation of lateral orbitofronto-striatal pathway suppresses compulsive behaviors. *Science (New York, N.Y.)*, *340*(6137), 1243–1246. https://doi.org/10.1126/science.1232380

Burguière, E., Monteiro, P., Feng, G., & Graybiel, A. M. (2013). Optogenetic stimulation of lateral orbitofronto-striatal pathway suppresses compulsive behaviors. *Science (New York, N.Y.)*, *340*(6137), 1243–1246. https://doi.org/10.1126/science.1232380

Cui, G., Jun, S. B., Jin, X., Pham, M. D., Vogel, S. S., Lovinger, D. M., & Costa, R. M. (2013). Concurrent activation of striatal direct and indirect pathways during action initiation. *Nature*, *494*(7436), 238–242. https://doi.org/10.1038/nature11846

Escabi, M. A., & Schreiner, C. E. (2002). Nonlinear spectrotemporal sound analysis by neurons in the auditory midbrain. *The Journal of Neuroscience : The Official Journal of the Society for Neuroscience*, *22*(10), 4114–4131. https://doi.org/20026325

Gage, G. J., Stoetzner, C. R., Wiltschko, A. B., & Berke, J. D. (2010). Selective Activation of Striatal Fast-Spiking Interneurons during Choice Execution. *Neuron*, *67*(3), 466–479. https://doi.org/10.1016/j.neuron.2010.06.034

Gittis, A. H., Nelson, A. B., Thwin, M. T., Palop, J. J., & Kreitzer, A. C. (2010). Distinct Roles of GABAergic Interneurons in the Regulation of Striatal Output Pathways. *Journal of Neuroscience*, *30*(6), 2223–2234. https://doi.org/10.1523/JNEUROSCI.4870-09.2010

Gradinaru, V., Zhang, F., Ramakrishnan, C., Mattis, J., Prakash, R., Diester, I., … Deisseroth, K. (2010). Molecular and cellular approaches for diversifying and extending optogenetics. *Cell*, *141*(1), 154–165. https://doi.org/10.1016/j.cell.2010.02.037

Guo, L., Walker, W. I., Ponvert, N. D., Penix, P. L., & Jaramillo, S. (2018). Stable representation of sounds in the posterior striatum during flexible auditory decisions. *Nature Communications*, *9*(1), 1534. https://doi.org/10.1038/s41467-018-03994-3

Hikosaka, O., & Wurtz, R. H. (1983). Visual and oculomotor functions of monkey substantia nigra pars reticulata. IV. Relation of substantia nigra to superior colliculus. *Journal of Neurophysiology*, *49*(5), 1285–1301. https://doi.org/10.1152/jn.1983.49.5.1285

Hintiryan, H., Foster, N. N., Bowman, I., Bay, M., Song, M. Y., Gou, L., … Dong, H.-W. (2016). The mouse cortico-striatal projectome. *Nature Neuroscience*, *19*(8), 1100–1114. https://doi.org/10.1038/nn.4332

Hippenmeyer, S., Vrieseling, E., Sigrist, M., Portmann, T., Laengle, C., Ladle, D. R., & Arber, S. (2005). A developmental switch in the response of DRG neurons to ETS transcription factor signaling. *PLoS Biology*, *3*(5), 0878–0890. https://doi.org/10.1371/journal.pbio.0030159

Hunnicutt, B. J., Jongbloets, B. C., Birdsong, W. T., Gertz, K. J., Zhong, H., & Mao, T. (2016). A comprehensive excitatory input map of the striatum reveals novel functional organization. *ELife*, *5*. https://doi.org/10.7554/eLife.19103

Joachimsthaler, B., Uhlmann, M., Miller, F., Ehret, G., & Kurt, S. (2014). Quantitative analysis of neuronal response properties in primary and higher-order auditory cortical fields of awake house mice (Mus musculus). *European Journal of Neuroscience*, *39*(6), 904–918. https://doi.org/10.1111/ejn.12478

Kemp, J. M., & Powell, T. P. S. (1971). The Structure of the Caudate Nucleus of the Cat: Light and Electron Microscopy. *Philosophical Transactions of the Royal Society B: Biological Sciences*, *262*(845), 383–401. https://doi.org/10.1098/rstb.1971.0102

Kim, J., Kim, Y., Nakajima, R., Shin, A., Jeong, M., Park, A. H., … Kim, D. (2017). Inhibitory Basal Ganglia Inputs Induce Excitatory Motor Signals in the Thalamus. *Neuron*, *95*(5), 1181-1196.e8. https://doi.org/10.1016/J.NEURON.2017.08.028

Kincaid, A. E., Zheng, T., & Wilson, C. J. (1998). Connectivity and convergence of single corticostriatal axons. *The Journal of Neuroscience : The Official Journal of the Society for Neuroscience*, *18*(12), 4722–4731. https://doi.org/10.1523/JNEUROSCI.18-12-04722.1998

Kincaid, A. E., Zheng, T., & Wilson, C. J. (1998). Connectivity and Convergence of Single Corticostriatal Axons. *J. Neurosci.*, *18*(12), 4722–4731. Retrieved from http://www.jneurosci.org/content/18/12/4722.long

Kita, H. (1993). GABAergic circuits of the striatum. *Progress in Brain Research*, *99*(C), 51–72. https://doi.org/10.1016/S0079-6123(08)61338-2

Koós, T., & Tepper, J. M. (1999). Inhibitory control of neostriatal projection neurons by GABAergic interneurons. *Nature Neuroscience*, *2*(5), 467–472. https://doi.org/10.1038/8138

Koós, T., & Tepper, J. M. (1999). Inhibitory control of neostriatal projection neurons by GABAergic interneurons. *Nature Neuroscience*, *2*(5), 467–472. https://doi.org/10.1038/8138

Kravitz, A. V., Freeze, B. S., Parker, P. R. L., Kay, K., Thwin, M. T., Deisseroth, K., & Kreitzer, A. C. (2010). Regulation of parkinsonian motor behaviours by optogenetic control of basal ganglia circuitry. *Nature*, *466*(7306), 622–626. https://doi.org/10.1038/nature09159

Lalive, A. L., Lien, A. D., Roseberry, T. K., Donahue, C. H., & Kreitzer, A. C. (2018). Motor thalamus supports striatum-driven reinforcement. *ELife*, *7*. https://doi.org/10.7554/eLife.34032

Lapper, S. R., Smith, Y., Sadikot, A. F., Parent, A., & Bolam, J. P. (1992). Cortical input to parvalbumin-immunoreactive neurones in the putamen of the squirrel monkey. *Brain Research*, *580*(1–2), 215–224. https://doi.org/10.1016/0006-8993(92)90947-8

Lee, A. T., Vogt, D., Rubenstein, J. L., & Sohal, V. S. (2014). A class of GABAergic neurons in the prefrontal cortex sends long-range projections to the nucleus accumbens and elicits acute avoidance behavior. *The Journal of Neuroscience : The Official Journal of the Society for Neuroscience*, *34*(35), 11519–11525. https://doi.org/10.1523/JNEUROSCI.1157-14.2014

Lee, K., Holley, S. M., Shobe, J. L., Chong, N. C., Cepeda, C., Levine, M. S., & Masmanidis, S. C. (2017). Parvalbumin Interneurons Modulate Striatal Output and Enhance Performance during Associative Learning. *Neuron*, *93*(6), 1451-1463.e4. https://doi.org/10.1016/j.neuron.2017.02.033

Lee, S.-H., Kwan, A. C., Zhang, S., Phoumthipphavong, V., Flannery, J. G., Masmanidis, S. C., … Dan, Y. (2012). Activation of specific interneurons improves V1 feature selectivity and visual perception. *Nature*, *488*(7411), 379–383. https://doi.org/10.1038/nature11312

Lesage, F. (2003). Pharmacology of neuronal background potassium channels. *Neuropharmacology*, *44*(1), 1–7. Retrieved from http://www.ncbi.nlm.nih.gov/pubmed/12559116

Li, L.-Y., Xiong, X. R., Ibrahim, L. A., Yuan, W., Tao, H. W., & Zhang, L. I. (2015). Differential Receptive Field Properties of Parvalbumin and Somatostatin Inhibitory Neurons in Mouse Auditory Cortex. *Cerebral Cortex (New York, N.Y. : 1991)*, *25*(7), 1782–1791. https://doi.org/10.1093/cercor/bht417

Lin, J. Y., Knutsen, P. M., Muller, A., Kleinfeld, D., & Tsien, R. Y. (2013). ReaChR: a red-shifted variant of channelrhodopsin enables deep transcranial optogenetic excitation. *Nature Neuroscience*, *16*(10), 1499–1508. https://doi.org/10.1038/nn.3502

Long, M. A., & Fee, M. S. (2008). Using temperature to analyse temporal dynamics in the songbird motor pathway. *Nature*, *456*(7219), 189–194. https://doi.org/10.1038/nature07448

Madisen, L., Zwingman, T. A., Sunkin, S. M., Oh, S. W., Zariwala, H. A., Gu, H., … Zeng, H. (2010). A robust and high-throughput Cre reporting and characterization system for the whole mouse brain. *Nature Neuroscience*, *13*(1), 133–140. https://doi.org/10.1038/nn.2467

Mallet, N., Le Moine, C., Charpier, S., & Gonon, F. (2005). Feedforward inhibition of projection neurons by fast-spiking GABA interneurons in the rat striatum in vivo. *The Journal of Neuroscience : The Official Journal of the Society for Neuroscience*, *25*(15), 3857–3869. https://doi.org/10.1523/JNEUROSCI.5027-04.2005

Mathis, A., Mamidanna, P., Cury, K. M., Abe, T., Murthy, V. N., Mathis, M. W., & Bethge, M. (2018). DeepLabCut: markerless pose estimation of user-defined body parts with deep learning. *Nature Neuroscience*, *21*(9), 1281–1289. https://doi.org/10.1038/s41593-018-0209-y

Mattis, J., Tye, K. M., Ferenczi, E. A., Ramakrishnan, C., O'Shea, D. J., Prakash, R., … Deisseroth, K. (2012). Principles for applying optogenetic tools derived from direct comparative analysis of microbial opsins. *Nature Methods*, *9*(2), 159–172. https://doi.org/10.1038/nmeth.1808

O'Hare, J. K., Li, H., Kim, N., Gaidis, E., Ade, K., Beck, J., … Calakos, N. (2017). Striatal fast-spiking interneurons selectively modulate circuit output and are required for habitual behavior. *ELife*, *6*, 1–26. https://doi.org/10.7554/eLife.26231

Owen, S. F., Berke, J. D., & Kreitzer, A. C. (2018). Fast-Spiking Interneurons Supply Feedforward Control of Bursting, Calcium, and Plasticity for Efficient Learning. *Cell*, *172*(4), 683-695.e15. https://doi.org/10.1016/j.cell.2018.01.005

Parthasarathy, H. B., & Graybiel, A. M. (1997). Cortically driven immediate-early gene expression reflects modular influence of sensorimotor cortex on identified striatal neurons in the squirrel monkey. *The Journal of Neuroscience : The Official Journal of the Society for Neuroscience*, *17*(7), 2477–2491. https://doi.org/10.1523/JNEUROSCI.17-07-02477.1997

Patel, A. J., & Honoré, E. (2001). Properties and modulation of mammalian 2P domain K+ channels. *Trends in Neurosciences*, *24*(6), 339–346. Retrieved from http://www.ncbi.nlm.nih.gov/pubmed/11356506

Pi, H.-J., Hangya, B., Kvitsiani, D., Sanders, J. I., Huang, Z. J., & Kepecs, A. (2013). Cortical interneurons that specialize in disinhibitory control. *Nature*, *503*(7477), 521–524. https://doi.org/10.1038/nature12676

Pisanello, F., Mandelbaum, G., Pisanello, M., Oldenburg, I. A., Sileo, L., Markowitz, J. E., … Sabatini, B. L. (2017). Dynamic illumination of spatially restricted or large brain volumes via a single tapered optical fiber. *Nature Neuroscience*, *20*(8), 1180–1188. https://doi.org/10.1038/nn.4591

Planert, H., Szydlowski, S. N., Hjorth, J. J. J., Grillner, S., & Silberberg, G. (2010). Dynamics of Synaptic Transmission between Fast-Spiking Interneurons and Striatal Projection Neurons of the Direct and Indirect Pathways. *Journal of Neuroscience*, *30*(9), 3499–3507. https://doi.org/10.1523/JNEUROSCI.5139-09.2010

Pouille, F., & Scanziani, M. (2001). Enforcement of Temporal Fidelity in Pyramidal Cells by Somatic Feed-Forward Inhibition. *Science*, *293*(5532), 1159–1163. https://doi.org/10.1126/science.1060342

Pouille, F., Marin-Burgin, A., Adesnik, H., Atallah, B. V, & Scanziani, M. (2009). Input normalization by global feedforward inhibition expands cortical dynamic range. *Nature Neuroscience*, *12*(12), 1577–1585. https://doi.org/10.1038/nn.2441

Prüss, H., Derst, C., Lommel, R., & Veh, R. W. (2005). Differential distribution of individual subunits of strongly inwardly rectifying potassium channels (Kir2 family) in rat brain. *Molecular Brain Research*, *139*(1), 63–79. https://doi.org/10.1016/j.molbrainres.2005.05.006

Ramanathan, S., Hanley, J. J., Deniau, J.-M., & Bolam, J. P. (2002). Synaptic convergence of motor and somatosensory cortical afferents onto GABAergic interneurons in the rat striatum. *The Journal of Neuroscience : The Official Journal of the Society for Neuroscience*, *22*(18), 8158–8169. https://doi.org/10.1523/JNEUROSCI.22-18-08158.2002

Reig, R., & Silberberg, G. (2014). Multisensory Integration in the Mouse Striatum. *Neuron*, *83*(5), 1200–1212. https://doi.org/10.1016/J.NEURON.2014.07.033

Rock, C., Zurita, H., Wilson, C., & Apicella, A. J. (2016). An inhibitory corticostriatal pathway. *ELife*, *5*. https://doi.org/10.7554/eLife.15890

Rothwell, P. E., Fuccillo, M. V., Maxeiner, S., Hayton, S. J., Gokce, O., Lim, B. K., … Südhof, T. C. (2014). Autism-Associated Neuroligin-3 Mutations Commonly Impair Striatal Circuits to Boost Repetitive Behaviors. *Cell*, *158*(1), 198–212. https://doi.org/10.1016/j.cell.2014.04.045

Royer, S., Zemelman, B. V., Losonczy, A., Kim, J., Chance, F., Magee, J. C., & Buzsáki, G. (2012). Control of timing, rate and bursts of hippocampal place cells by dendritic and somatic inhibition. *Nature Neuroscience*, *15*(5), 769–775. https://doi.org/10.1038/nn.3077

Rymar, V. V., Sasseville, R., Luk, K. C., & Sadikot, A. F. (2004). Neurogenesis and stereological morphometry of calretinin-immunoreactive GABAergic interneurons of the neostriatum. *The Journal of Comparative Neurology*, *469*(3), 325–339. https://doi.org/10.1002/cne.11008

Sachidhanandam, S., Sermet, B. S., & Petersen, C. C. H. (2016). Parvalbumin-Expressing GABAergic Neurons in Mouse Barrel Cortex Contribute to Gating a Goal-Directed Sensorimotor Transformation. *Cell Reports*, *15*(4), 700–706. https://doi.org/10.1016/j.celrep.2016.03.063

Schneider, E. R., Anderson, E. O., Gracheva, E. O., & Bagriantsev, S. N. (2014). Temperature Sensitivity of Two-Pore (K2P) Potassium Channels. In *Current topics in membranes* (Vol. 74, pp. 113–133). https://doi.org/10.1016/B978-0-12-800181-3.00005-1

Smith, Y., Bevan, M. D., Shink, E., & Bolam, J. P. (1998). Microcircuitry of the direct and indirect pathways of the basal ganglia. *Neuroscience*, *86*(2), 353–387. https://doi.org/10.1016/S0306-4522(98)00004-9

Smith, Y., Bennett, B. D., Bolam, J. P., Parent, A., & Sadikot, A. F. (1994). Synaptic relationships between dopaminergic afferents and cortical or thalamic input in the sensorimotor territory of the striatum in monkey. *The Journal of Comparative Neurology*, *344*(1), 1–19. https://doi.org/10.1002/cne.903440102

Sohal, V. S., Zhang, F., Yizhar, O., & Deisseroth, K. (2009). Parvalbumin neurons and gamma rhythms enhance cortical circuit performance. *Nature*, *459*(7247), 698–702. https://doi.org/10.1038/nature07991

Steude, A., Witts, E. C., Miles, G. B., & Gather, M. C. (2016). Arrays of microscopic organic LEDs for high-resolution optogenetics. *Science Advances*, *2*(5), e1600061. https://doi.org/10.1126/sciadv.1600061

Straub, C., Saulnier, J. L., Bègue, A., Feng, D. D., Huang, K. W., & Sabatini, B. L. (2016). Principles of Synaptic Organization of GABAergic Interneurons in the Striatum. *Neuron*, *92*(1), 84–92. https://doi.org/10.1016/j.neuron.2016.09.007

Stujenske, J. M., Spellman, T., & Gordon, J. A. (2015). Modeling the Spatiotemporal Dynamics of Light and Heat Propagation for InVivo Optogenetics. *Cell Reports*, *12*(3), 525–534. https://doi.org/10.1016/j.celrep.2015.06.036

Tepper, J. M., Koó, T., & Wilson, C. J. (2004). GABAergic microcircuits in the neostriatum. *TRENDS in Neurosciences*, *27*(11). https://doi.org/10.1016/j.tins.2004.08.007

Wall, N. R., De La Parra, M., Callaway, E. M., & Kreitzer, A. C. (2013). Differential Innervation of Direct- and Indirect-Pathway Striatal Projection Neurons. *Neuron*, *79*(2), 347–360. https://doi.org/10.1016/j.neuron.2013.05.014

Wawrzkiewicz-Jałowiecka, A., Dworakowska, B., & Grzywna, Z. J. (2017). The temperature dependence of the BK channel activity – kinetics, thermodynamics, and long-range correlations. *Biochimica et Biophysica Acta (BBA) - Biomembranes*, *1859*(10), 1805–1814. https://doi.org/10.1016/j.bbamem.2017.05.013

Wehr, M., & Zador, A. M. (2003). Balanced inhibition underlies tuning and sharpens spike timing in auditory cortex. *Nature*, *426*(6965), 442–446. https://doi.org/10.1038/nature02116

Xiong, Q., Znamenskiy, P., & Zador, A. M. (2015). Selective corticostriatal plasticity during acquisition of an auditory discrimination task. *Nature*, *521*(7552), 348–351. https://doi.org/10.1038/nature14225

Yamamoto, S., Monosov, I. E., Yasuda, M., & Hikosaka, O. (2012). What and Where Information in the Caudate Tail Guides Saccades to Visual Objects. *Journal of Neuroscience*, *32*(32), 11005–11016. https://doi.org/10.1523/jneurosci.0828-12.2012

Yang, F., Cui, Y., Wang, K., & Zheng, J. (2010). Thermosensitive TRP channel pore turret is part of the temperature activation pathway. *Proceedings of the National Academy of*

Sciences of the United States of America, *107*(15), 7083–7088. https://doi.org/10.1073/pnas.1000357107

Yang, F., & Zheng, J. (2014). High temperature sensitivity is intrinsic to voltage-gated potassium channels. *ELife*, *3*, e03255. https://doi.org/10.7554/eLife.03255

Yizhar, O., Fenno, L. E., Davidson, T. J., Mogri, M., & Deisseroth, K. (2011). Optogenetics in Neural Systems. *Neuron*, *71*(1), 9–34. https://doi.org/10.1016/j.neuron.2011.06.004

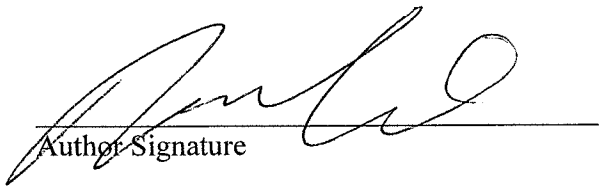
Znamenskiy, P., & Zador, A. M. (2013). Corticostriatal neurons in auditory cortex drive decisions during auditory discrimination. *Nature*, *497*(7450), 482–485. https://doi.org/10.1038/nature12077

Publishing Agreement

It is the policy of the University to encourage the distribution of all theses, dissertations, and manuscripts. Copies of all UCSF theses, dissertations, and manuscripts will be routed to the library via the Graduate Division. The library will make all theses, dissertations, and manuscripts accessible to the public and will preserve these to the best of their abilities, in perpetuity.

Please sign the following statement:

I hereby grant permission to the Graduate Division of the University of California, San Francisco to release copies of my thesis, dissertation, or manuscript to the Campus Library to provide access and preservation, in whole or in part, in perpetuity.



Author Signature

6/15/2019

Date